Paleoceanography and Paleoclimatology®

Key Points:

- Simulated equatorial surface ocean $p\mathrm{CO_2}$ is near-equilibrium with atmosphere during interglacials but enriched (≤ 35 ppm) during glacials
- Models suggest similar equatorial surface $p\mathrm{H}$ in Pacific and in Atlantic in high CO_2 worlds while Pliocene reconstructions show offsets
- Carbon cycle model analysis suggests that reported CO_2 values above 500 ppm in the Pliocene might need revisions to smaller numbers

Supporting Information:

Supporting Information may be found in the online version of this article.

Correspondence to:

P. Köhler,
Peter.Koehler@awi.de

Atmospheric CO₂ Concentration Based on Boron Isotopes Versus Simulations of the Global Carbon Cycle During the Plio-Pleistocene

Peter Köhler[1] 📙

[1]Alfred-Wegener-Institut Helmholtz-Zentrum für Polar-und Meeresforschung (AWI), Bremerhaven, Germany

Abstract Atmospheric carbon dioxide concentrations ($p\mathrm{CO_2}$) beyond ice core records have been reconstructed from $\delta^{11}\mathrm{B}$ derived from planktic foraminifera found in equatorial sediment cores. Here, I applied a carbon cycle model over the Plio-Pleistocene to evaluate the assumptions leading to these numbers. During glacials times, simulated atmospheric $p\mathrm{CO_2}$ was unequilibrated with $p\mathrm{CO_2}$ in the equatorial surface ocean by up to 35 ppm while the $\delta^{11}\mathrm{B}$-based approaches assume unchanged (quasi)equilibrium between both. In the Pliocene, $\delta^{11}\mathrm{B}$-based estimates of surface ocean $p\mathrm{H}$ are lower in the Pacific than in the Atlantic resulting in higher calculated $p\mathrm{CO_2}$. This offset in $p\mathrm{H}$ between ocean basins is not supported by models. To calculate $p\mathrm{CO_2}$ in surface waters out of the $\delta^{11}\mathrm{B}$-based $p\mathrm{H}$ some assumptions on either total alkalinity or dissolved inorganic carbon are necessary. However, the assumed values of these under-constrained variables were according to my results partly inconsistent with chemically possible combinations within the marine carbonate system. The model results show glacial/interglacial variability in total alkalinity of the order of 100 μmol/kg, which is rarely applied to proxy reconstructions. Simulated atmospheric $p\mathrm{CO_2}$ is tightly ($r^2 > 0.9$) related to equatorial surface-ocean $p\mathrm{H}$, which can be used for consistency checks. Long-term trends in volcanic CO_2 outgassing and the strength of the continental weathering fluxes are still unconstrained, allowing for a wide range of possible atmospheric $p\mathrm{CO_2}$ across the Plio-Pleistocene. Nevertheless, this carbon cycle analysis suggests that reported atmospheric $p\mathrm{CO_2}$ above 500 ppm in the Pliocene might, for various reasons, need to be revised to smaller numbers.

1. Introduction

Although carbon dioxide (CO_2) is one of the most important greenhouse gases, our knowledge of its atmospheric concentration beyond the 800 ka covered by ice cores (Bereiter et al., 2015) is highly uncertain (Figure 1a). Data obtained from blue ice in the Allan Hills, Antarctica, provide three snapshots of CO_2 with values between 200 and 280 ppm at roughly 1.0, 1.5, and 2.0 Ma (Yan et al., 2019). In comparison, reconstructions based on marine proxies ($\delta^{11}\mathrm{B}$ (Bartoli et al., 2011; Chalk et al., 2017; de la Vega et al., 2020; Dyez et al., 2018; Foster, 2008; Guillermic et al., 2022; Henehan et al., 2013; Hönisch et al., 2009; Martínez-Botí et al., 2015; Seki et al., 2010), alkenones (Badger et al., 2013, 2019; Seki et al., 2010; Zhang et al., 2013)), paleosol (Da et al., 2019) or leaf wax $\delta^{13}\mathrm{C}$ (Yamamoto et al., 2022) are temporally higher resolved and span a wide range of possible Plio-Pleistocene CO_2 histories, from concentrations of approximately 180 ppm typical for late Pleistocene glacials to in general up to 500 ppm in the Pliocene, with some exceptions showing up to 600 ppm. Thus, it is still unclear what role changes in CO_2 radiative forcing played during major climate transitions of the last 5 Ma, for example, the initiation of northern hemisphere glaciation (e.g., Raymo, 1994) or the intensification of glacial/interglacial (G/IG) amplitudes and the change in the periodicity of interglacial periods across the so-called Mid-Pleistocene Transition (Berends et al., 2021; Köhler & van de Wal, 2020). Furthermore, mid-Pliocene climate (~3.3–3.0 Myr BP) is typically considered as an analog to evaluate the sensitivity of the climate to future CO_2 concentrations, which is only of limited value if the chosen atmospheric CO_2 concentration during Earth system model experiments is only weakly supported by data (Haywood et al., 2016).

One of the most prominent CO_2 proxies is based on boron isotopes measured in planktic foraminifera. It has been posited (Dyez et al., 2018) that the resulting atmospheric CO_2 concentration is partly species-specific; for example, reconstructions based on *T. sacculier* are different from those based on *G. ruber*. Other comparative studies have also identified a constant offset between different measurement techniques (Farmer et al., 2016; Foster et al., 2013; Hönisch et al., 2019a). For a comprehensive understanding of these differences, and for a better
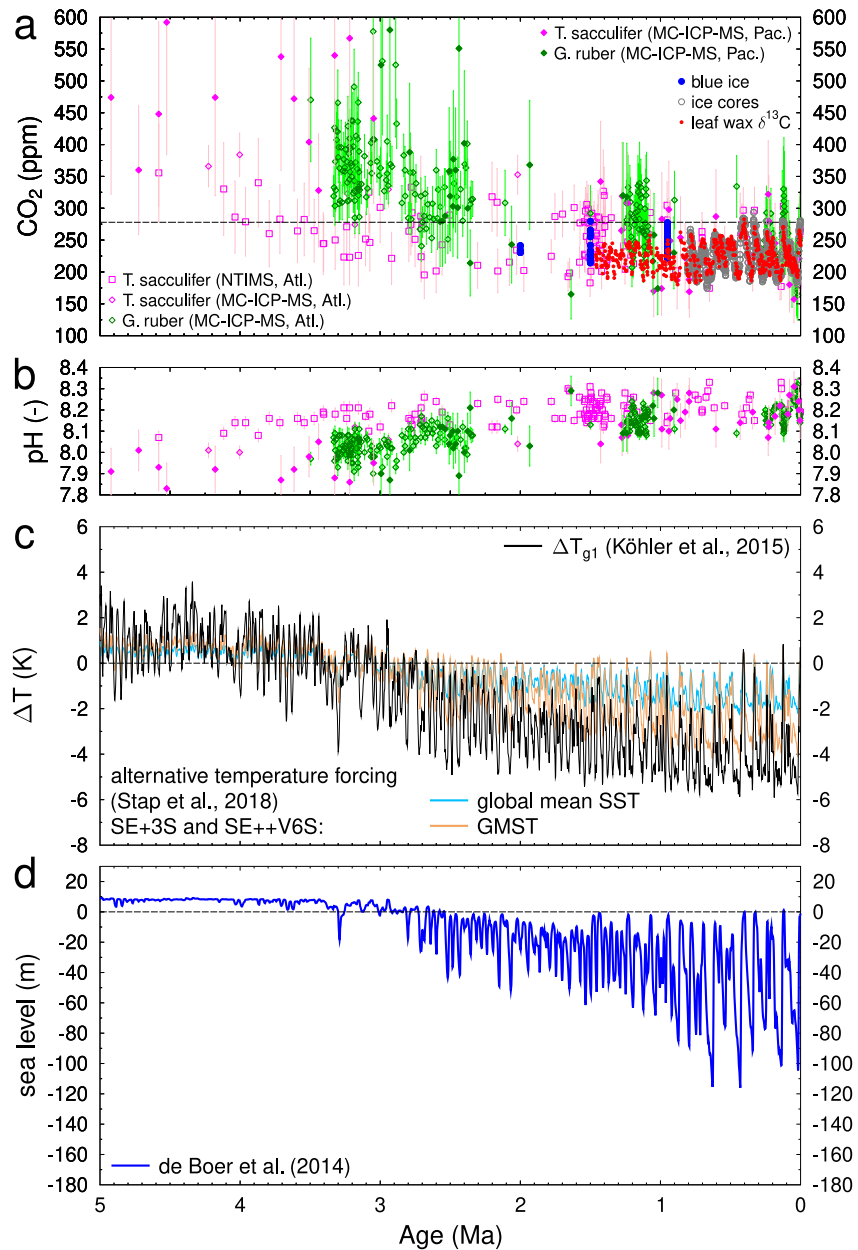
Figure 1. Climate reconstructions over the past 5 Ma. (a) Atmospheric CO_2 concentration and (b) surface water pH reconstructed from δ^{11}B, distinguished by species, method and ocean basin (Atlantic: open symbols; Pacific: filled symbols). Based on Atlantic cores as compiled in Dyez et al. (2018) with updates from de la Vega et al. (2020) and Pacific core as in Guillermic et al. (2022); In (a) additionally data from ice cores (Bereiter et al., 2015), blue ice (Yan et al., 2019) and leaf wax δ^{13}C (Yamamoto et al., 2022) are plotted. (c) Global temperature changes: ΔT_{g1} is taken from (Köhler et al., 2015b) and represents a global mean surface temperature (GMST), alternative data from Stap et al. (2018a) (GMST; global mean sea surface temperature) are taken; (d) Sea level (de Boer et al., 2014). Error bars show 1σ uncertainties.

understanding of this proxy, one needs to be aware that the measured δ^{11}B data are transferred into pH using species- and technique-specific proxy calibrations. Thus, δ^{11}B applied as a pH proxy contains also difficulties which come along with proxies in general, such as clay contamination, diagenesis, updates in calibration methods, or offsets between laboratory and natural measurements (e.g., Hönisch et al., 2019a, 2019b). A second variable of the marine carbonate system is necessary for the estimation of the CO_2 partial pressure. The applied methods include the approximation of total alkalinity (TA), some times based on salinity under the assumption that the globally integrated TA in the ocean remained constant in the past. Alternatively, several long-term trends in TA

based on various other studies have been tested in Guillermic et al. (2022), while de la Vega et al. (2020) used dissolved inorganic carbon (DIC) as reconstructed out of other marine data (Sosdian, Greenop, et al., 2018) as the second variable of the marine carbonate system. Furthermore, as this approach only reconstructs the changes in the carbonate chemistry of the surface ocean, it is necessary that the sediment cores from where planktic species are extracted are located in areas wherein the CO_2 partial pressure of the surface ocean and the atmosphere are in (or near) equilibration or where at least its difference is rather constant over time. Most relevant data published for the Plio-Pleistocene was compiled in one overview (Dyez et al., 2018) and were obtained from two marine sediment cores (Ocean Drilling Program (ODP) sites 668 or 999) in the equatorial Atlantic. Another recent study (Guillermic et al., 2022) uses material from ODP 806 and 807 in the equatorial Pacific. This near-equilibrium condition is fulfilled for the equatorial regions in both ocean basins for a preindustrial (PI) climate. During proxy interpretation, it is now generally assumed that the surface ocean-atmosphere equilibrium remained unchanged.

In this study, I use the global carbon cycle model BICYCLE-SE (Köhler & Munhoven, 2020b) and analyze transient simulation results across the Plio-Pleistocene and compare these results to CO_2 reconstructions based on $\delta^{11}B$ from planktic foraminifera. In-depth rationale for applied late Pleistocene forcing and an analysis of G/IG changes in the carbon cycle can be found in earlier papers (Köhler & Munhoven, 2020b; Köhler et al., 2005, 2010). The main philosophy of the approach can be condensed in what others (e.g., Brovkin et al., 2007) call the CO_2 *stew*: since there is not a single plausible process that can be made responsible for the observed changes one needs to consider a variety of processes, for which evidence of their changes over time exist and implement them in a model including physical boundary conditions (ocean circulation, temperature, sea level, sea ice), biogeochemistry (carbonate compensation, marine carbon pumps, land carbon storage), and additionally, since the last model extension, solid Earth processes (volcanic CO_2 outgassing, weathering, shallow water $CaCO_3$ sink via coral reefs). The model simulates the full marine carbonate chemistry, including the carbon isotopes, and contains in its newest version a process-based sediment module. Thus, the plausibility of typical assumptions made during proxy-based CO_2 reconstructions can be checked within a carbon cycle modeling framework.

2. Methods

2.1. The Global Carbon Cycle Model BICYCLE-SE

In this study BICYCLE, a box model of the global carbon cycle (Köhler & Munhoven, 2020b; Köhler et al., 2010) is used. BICYCLE consists of ten ocean boxes, one global averaged atmosphere, and a terrestrial biosphere that distinguishes C_3 or C_4 photosynthesis in grasses and trees, and soil carbon with different turnover times. The terrestrial carbon content varies as a consequence of CO_2 fertilization and temperature-dependent respiration (Köhler & Fischer, 2004). In the ocean, the marine carbonate system is explicitly calculated (Zeebe & Wolf-Gladrow, 2001), tracing DIC and TA, from which as functions of temperature, salinity, and pressure, the other variables of the marine carbonate system (dissolved CO_2, HCO_3^-, CO_3^{2-}, pH) were calculated by using the dissociation constants pK_1 and pK_2 of Mojica Prieto and Millero (2002). Marine export production is a function of macro nutrients at the surface ocean, which is for PI climate restricted to 10 PgC/yr, corresponding to results of more complex ocean general circulation models (e.g., Schlitzer, 2000). This leads to unused nutrients, particularly in the Southern Ocean, which could be used for primary production if prescribed iron fluxes indicate that iron is no longer a limited micronutrient. All temporal changes in climate (e.g., temperature, salinity, ocean circulation, and sea ice) are prescribed externally. Recently, solid Earth processes (process-based sediments for exchange fluxes of $CaCO_3$ between the deep ocean and the ocean sediments, volcanic CO_2 outgassing, silicate and carbonate weathering as riverine inputs of bicarbonate, and coral reefs as another shallow water sink of $CaCO_3$) have been implemented in BICYCLE, version SE (Köhler & Munhoven, 2020b), which is the version used here (Figure S1 in Supporting Information S1). Both weathering fluxes bring alkalinity and carbon into the ocean at a ratio of 1:1, but while all carbon comes from atmospheric CO_2 in silicate weathering, during carbonate weathering its sources are 50% each in atmospheric CO_2 and carbonate rock.

For the transient application of the model over the last 5 Ma, BICYCLE-SE is forced using changing climatic boundary conditions derived from published time series. I use sea level (Figure 1d) as obtained from the model-based deconvolution of the global mean benthic $\delta^{18}O$ stack LR04 (de Boer et al., 2014; Lisiecki & Raymo, 2005). Ocean salinity changes as a function of sea level (Figure S2a in Supporting Information S1). Two alternative approaches are followed for the forced temperature changes, which roughly bracket existing published estimates. First, the global mean surface temperature (GMST) obtained as ΔT_{g1} in Köhler et al. (2015b), which

is a follow-up and based on de Boer et al. (2014), is used. Second, simulated temperature time series from the scenario OIC, in which changes in orbital forcing (O), ice sheets (I) and CO_2 (C) were prescribed, performed with the CLIMBER model as published in Stap et al. (2018a) are taken. Here, not only GMST, but also global mean and regional sea surface temperature (SST) values (south of 40°S; 40°S–40°N; north of 40°N) have been extracted from the simulation results. The temperature time series of both approaches agree in their general form since they both use, in different ways, information from the LR04 $\delta^{18}O$. However, they differ in their G/IG amplitudes with generally larger amplitudes in the approach of Köhler et al. (2015b) than in the one using Stap et al. (2018a), for example, at Last Glacial Maximum (LGM) the change in GMST is either −5.7 K or −4.1 K, respectively (Figure 1c). When using GMST from Köhler et al. (2015b) this time series is applied to all boxes (surface and deep ocean, land vegetation), while when using data from Stap et al. (2018a) GMST is applied on the land carbon cycle, regional SST to the surface boxes and mean ocean SST to the deep ocean, the latter based on the evidence that mean ocean temperature (Haeberli et al., 2021) and global mean SST (Tierney et al., 2020) during the LGM have both been reconstructed to be around −3 K. I acknowledge that temperature time series used here are potentially different from other reconstructions (e.g., the CLIMBER model output of Stap et al. (2018a) finds a mean SST at LGM of only −2 K), but continue with them nevertheless since they are published and follow from assumptions outlined in the relevant papers. Thus, using two different approaches here (Köhler et al., 2015b; Stap et al., 2018a) should illustrate how a detailed knowledge of temperature change influences the simulated global carbon cycle. A more in-depth discussion of the consequences of alternative temperature and sea level forcing for the global carbon cycle, that agree more closely with independent data is planned in future work based on a not yet published SST compilation across the last 4.5 Ma (Clark et al., 2021).

Based on LGM and PI reconstructions (Cavalieri et al., 1997; Gersonde et al., 2005; Sarnthein et al., 2003), sea ice was linearly interpolated as a function of local SST (Figure S2e in Supporting Information S1). Using the same relationship for a warmer-than-PI climate might be a bold simplification, but for the simulated carbon cycle in the model, it is rather unimportant, because it primarily influences atmospheric CO_2 if the high-latitude ocean boxes are largely covered by sea ice (see Köhler & Fischer, 2006, for details). North Atlantic Deep Water (NADW) formation and subsequent Atlantic meridional overturning circulation (AMOC) were assumed to follow either an interglacial or glacial mode with 16 or 10 Sv for NADW formation, respectively. These values were for PI (interglacial) climate constrained from the World Ocean Circulation Experiment data (Ganachaud & Wunsch, 2000) and were for the glacial model based on various modeling studies (e.g., Meissner et al., 2003). The switch between both states was related to the NH high-latitude SST (Figure S2b in Supporting Information S1). Again, this is largely simplified; however, simulations with more complex models of the Mid-Pliocene AMOC are inconclusive but suggest only slightly larger overturning during Mid-Pliocene interglacials than during PI (Zhang et al., 2021). Southern Ocean vertical mixing is traditionally used in the BICYCLE model as a function of SH high-latitude SST (Figure S2c in Supporting Information S1). Again, as this has been parameterized to distinguish glacial from interglacial states in the late Pleistocene, this exchange is restricted to its values prescribed for PI and LGM conditions to vary between 29 and 9 Sv. Iron input (Fe mass accumulation rate (MAR)) from ODP 1090 covering the last 4 Myr (Martinez-Garcia et al., 2011) was used to prescribe changes in marine export production in the Southern Ocean. Here, as done in previous applications of the BICYCLE model, the value of Fe MAR at 18 ka BP, the time when CO_2 starts to rise during Termination I, was used to mark the threshold when the system switched from an iron-unlimited regime in which all macro nutrients were used by biological productivity, to an iron-limited regime in which the global export production was restricted to its strength during PI (Figure S2d in Supporting Information S1). Since Fe MAR at the start of the time series is well below this threshold starting its consideration only at 4 Ma does no lead to abrupt changes in the simulations. Furthermore, as described in more details below, results before 4 Ma are less reliable being considered an evolving spin-up.

In addition to the change in the applied forcing time series, the model had to be adapted in one specific aspect: based on a comparison of LGM and PI (Börker et al., 2020) the weathering fluxes were kept constant over time in version SE used in Köhler and Munhoven (2020a). However, applying the forcing (Figure S2 in Supporting Information S1), this would lead to unrealistic low CO_2 values for the late Pleistocene, the time period for which ice core data provide good constraints. I therefore updated the model by using two different realizations of weathering fluxes W being a function of CO_2, following

$$W = W_0 \left(\frac{CO_2}{CO_{2,0}} \right)^{n_X}, \tag{1}$$

with either $n_X = 0.075$ for both silicate and carbonate weathering. or $n_{Si} = 0.2$ and $n_{Ca} = 0.4$ for silicate and carbonate weathering, respectively. Here, W_0 and $CO_{2,0}$ are the PI flux rate and CO_2 concentration, respectively. The first realization is called a *weak*, the second realization a strong weathering approach. They are labeled SE+ and SE++, respectively. In the original version of SE, in which weathering is independent from CO_2, n was set to 0. Equation 1 was taken, including the parameterization for strong weathering, from Zeebe (2012), but has been used before (e.g., Berner et al., 1983). It has been found that runoff and temperature are the most important climate variables which determine the strength of weathering fluxes (Hartmann et al., 2009, 2014). Equation 1 condenses this finding into a dependency of CO_2 to be easily applicable in simple models. The chosen values for n in weak weathering were obtained from the simulation results to fit the late Pleistocene ice core CO_2 without assuming any changes in volcanic CO_2 outgassing over time. In its strong form, the weathering feedback had been compared, and agreed well with results based on the interpretation of typically weathering proxies, such as the isotopes of Sr, Li, Os, over the Cenozoic (Caves et al., 2016). Furthermore, the strong weathering feedback has already been applied to long-term future emission scenarios calculated with BICYCLE-SE (Köhler, 2020).

2.2. Scenarios

In the initial setup (scenario SE+0) BICYCLE-SE is run with weak CO_2-dependency of weathering fluxes. Further refinement are performed as follows: First (scenario SE+1), the impact of the gradual long-term trend in mean ocean Mg and Ca concentrations on the marine carbonate system was considered. Concentrations in Mg and Ca of 48 mmol/kg and 11 mmol/kg respectively at 5 Ma are assumed, which gradually and linearly changed toward their present-day values (Mg: 52.8 mmol/kg; Ca: 10.3 mmol/kg) (Zeebe & Tyrrell, 2019). The corrections of the marine carbonate system caused by changes in Mg and Ca were calculated using the MyAMI model (Hain, Sigman, et al., 2018; Hain et al., 2015), leading to a nearly 10 ppm long-term decrease in CO_2 over time (Figure S3b in Supporting Information S1). Recently, it has been suggested that the mean ocean Ca concentration might be as high as 13 mmol/kg at 5 Ma (Zhou et al., 2021). Such changes implemented in the model would contribute to 20 ppm decline in CO_2 between 4.8 Ma and 3 Ma (scenario SE+4, Figure S3b in Supporting Information S1). However, this would also change the Mg/Ca ratio at 5 Ma to 3.7, a value that is not completely impossible, but according to reconstructions rather unlikely (Evans et al., 2016). I therefore kept changes in Ca between 11 mmol/kg and 10.3 mmol/kg.

Second (scenario SE+2), it was realized in the previous scenarios that simulated G/IG amplitudes not only of CO_2 but also of mean ocean $\delta^{13}C$ are considerably smaller before than after the Mid Pleistocene Transition, while existing $\delta^{13}C$ data (Lisiecki, 2014; Poore et al., 2006) do not provide indications for such strong changes (Figure S4 in Supporting Information S1). Such a model/data disagreement in $\delta^{13}C$ has also been observed in previous simulations covering the last 2 Ma (Köhler & Bintanja, 2008) and has led to the Southern Ocean Decoupling Hypothesis, which suggested that before the Mid Pleistocene Transition, the Southern Ocean deep-ocean circulation was not directly related to sea surface temperature. Here, a different approach is followed. Alternatively in scenario SE+2 the Southern Ocean vertical mixing flux is calculated as a function of sea level (Figure 1d). Further evidence for such a revision of the forcing comes from studies that show that water density, which is important for vertical water mass changes, depends more on the salinity of the Southern Ocean than on temperature (Knorr et al., 2021; Terhaar et al., 2021). Here, the extrapolation of the Southern Ocean mixing term beyond the values chosen for PI and LGM were avoided, implying that sea level lower than LGM (and higher than PI) has no further impacts (Figure S2c in Supporting Information S1). This approach has only a small impact on CO_2 G/IG amplitudes found here (see SE+0 vs. SE+3 in Figure S3a in Supporting Information S1) but is potentially of interest in future runs with alternative forcing in which G/IG amplitudes in sea level and temperature vary differently across the Mid Pleistocene Transition (Clark et al., 2021). Furthermore, using sea level to force Southern Ocean vertical mixing makes this flux independent from the two different temperature approaches. The mean ocean $\delta^{13}C$ G/IG amplitudes are also only little affected (Figure S4 in Supporting Information S1).

Third (scenario SE+3), it was found that in the early part of the simulation window, when the sea level was primarily above the PI levels, the simulated mean ocean $\delta^{13}C$ was consistently higher than the reconstructions (Figure S4c in Supporting Information S1). It was found that the $CaCO_3$ accumulation in coral reefs, which was realized with an isotopic fractionation of $-2‰$ with respect to $\delta^{13}C$ of DIC in the surface ocean (Felis et al., 2022; Linsley et al., 2019), was primarily responsible for this offset. In scenario SE+3, this $\delta^{13}C$ mismatch was improved by restricting coral reef growth for higher than present day sea level to half its otherwise possible

Table 1
Simulation Scenarios Investigated Here

Acronym	Description
SE+0	Solid Earth version with weak CO_2-dependency of weathering fluxes
SE+1	As SE+0, but impact of time-dependent change in Mg and Ca on carbonate chemistry considered with Ca = 11 mmol/kg and Mg = 48 mmol/kg at 5 Ma
SE+2	As SE+1, but Southern Ocean vertical mixing is now a function of sea level (and not of SST as before)
SE+3	As SE+2, but coral growth for sea level >0 revised
SE+4	As SE+3, but with Ca = 13 mmol/kg at 5 Ma (Zhou et al., 2021)
SE+V2	As SE+3, but with 2% long-term decline in volcanic CO_2 outgassing between 4.5 and 1.0 Ma
SE+V4	As SE+3, but with 4% long-term decline in volcanic CO_2 outgassing between 4.5 and 1.0 Ma
SE+V6	As SE+3, but with 6% long-term decline in volcanic CO_2 outgassing between 4.5 and 1.0 Ma
SE++V6	As SE+V6, but with strong CO_2-dependency of weathering fluxes
SE++V12	As SE++V6, but with 12% long-term decline in volcanic CO_2 outgassing between 4.5 and 1.0 Ma
SE++V18	As SE++V6, but with 18% long-term decline in volcanic CO_2 outgassing between 4.5 and 1.0 Ma

Note. In the standard setup the temperature forcing of is used. For various additional simulations the alternative temperature forcing (Stap et al., 2018a) is applied, which is marked in figures and discussions by the extension of acronym by "S," for example, SE+3S instead of SE+3.

value. This adjustment reduced the long-term $CaCO_3$ sink in corals before 3 Ma by more than 1 Tmol/yr (see magenta lines for SE+0 vs. SE++V6 in Figure S5b and S5c in Supporting Information S1). This final correction in coral reef growth implemented in SE+3 (and various other scenarios such as SE++V6) reduced CO_2 before 3 Ma and roughly compensated for the effects of Mg and Ca changes over time introduced in SE+1 (Figure S3b in Supporting Information S1). I acknowledge that after ~2.7 Ma simulated mean ocean $\delta^{13}C$ in most scenarios slightly increases over time, while the data compilation shows the opposite (Figures S4c–S4e in Supporting Information S1). Here, I try not to further reduce this data/model offset in mean ocean $\delta^{13}C$. This is postponed to future studies, since first results based on sea level and temperature time series of Clark et al. (2021) indicate a solution to this problem. Here, mainly large G/IG amplitudes in sea level as early as 2.5 Ma in this alternative forcing lead to differences in coral reef growth having due to the assumed isotopic fractionation during $CaCO_3$ formation a direct effect on $\delta^{13}C$ in the simulated marine carbon cycle.

With these three adjustments all included in SE+3, this scenario can be considered as the standard run, which contained all implemented solid Earth processes including G/IG changes (but no long-term trend) in volcanic CO_2 and a weak weathering strength. However, owing to the lingering uncertainty in the knowledge of these two processes, a few more scenarios were added in which they were modified slightly. For example, Willeit et al. (2019) argued for a 20% decrease in volcanic CO_2 release between 3 Ma and 1 Ma. Volcanic CO_2 release gradually decreased between 4.5 and 1 Ma by up to 18% in either setup with weak or strong weathering strength, adding six more scenarios. Simulated CO_2 covered roughly the range of values found in the proxy-based reconstructions, including values larger than 500 ppm at approximately 3.5 Ma (Figure S3a in Supporting Information S1).

An overview of all the simulated scenarios is presented in Table 1. In the standard case temperature forcing follows Köhler et al. (2015b), while scenarios in which temperatures are based on Stap et al. (2018a) are marked in their label with an "S" at the end, for example, SE+V3 and SE+V3S, respectively. Because of the long-term effects of different weathering/volcanic emissions scenarios, all simulation results before 4 Ma are considered as a type of evolving spin-up, and I only discuss results later than this point in time. In most figures, a vertical line at 4 Ma clearly marks the end of this spin-up period.

The long-term (400 ka-running mean) contributions of the different non-solid Earth processes (changes in temperature, sea level, sea ice, NADW, Southern Ocean vertical mixing, iron fertilization of the Southern Ocean, terrestrial carbon storage) to changes in simulated atmospheric CO_2 are briefly analyzed for the standard scenario SE+3 (Figure S6 in Supporting Information S1). The dominant CO_2 decrease over the last 5 Ma of about 35 ppm is caused by temperature change, while I obtain roughly half of that number if the temperature forcing from Stap et al. (2018a) is applied. Terrestrial carbon, sea level and sea ice lead to little changes, while Southern Ocean processes and large scale ocean circulation changes connected with the NADW contribute to a reduction of up to 15 ppm.

Table 2
Overview on Main Findings and an Estimate of Their Robustness and How They Are Supported by Other Studies

Finding	Description	Robustness
Glacial bias	Disequilibrium of pCO$_2$ between equatorial waters and atmosphere during glacial times, caused by polar processes being partly responsible for glacial CO$_2$ drawdown (see also Bouttes et al., 2011; Menviel et al., 2017).	More likely than not, agreements among models (Kurahashi-Nakamura et al., 2022; Völker & Köhler, 2013) for ODP668 and Pacific sites, disagreements for ODP999, but only little glacial CO$_2$ drawdown in Völker and Köhler (2013).
Equatorial pH	Surface ocean pH in Atlantic and Pacific in a high CO$_2$ world should be very similar.	Robust, unless ocean circulation regime is completely different; supported by modern data and future projections (Jiang et al., 2019).
2nd parameter	Assumptions made for the second parameter of the marine carbonate system needs to be in agreement with chemically possible combinations.	Robust, based on C cycle internal knowledge derived from decades of laboratory measurements; can be tested with any global carbon cycle model.
Glacial/interglacial	Simulated glacial/interglacial changes in global carbon cycle, including atmospheric CO$_2$, all variables of the marine carbonate system and ^{13}C.	To some degree model-specific, but supported by agreement with independent data; glacial/interglacial amplitudes in all variables in the Pliocene are probably too small (Lisiecki, 2014; Poore et al., 2006).
Long-term trend	Weathering feedback strength and volcanic CO$_2$ outgassing determining the long-term trend in the carbon cycle including atmospheric CO$_2$.	Strong weathering feedback agrees with independent proxies (Caves et al., 2016), temporal change in volcanic CO$_2$ outgassing largely unknown.

3. Results

Before analyzing the situation of the carbon cycle in the surface equatorial regions, the areas in which the sediment cores were retrieved from which all the δ^{11}B-based CO$_2$ reconstructions considered here were obtained, and provide further model-based insights, I examine long-term model performance by investigating deep ocean changes in the carbon cycle. The main findings of the whole study, including judgments on robustness and independent support, are summarized in Table 2.

3.1. Long-Term Deep Ocean Carbon Cycle

The general G/IG marine carbon cycle dynamics of the model included variations in the calcite saturation horizons (CSH) in the order of 1 km and deep ocean CO$_3^{2-}$ anomalies of 10–20 μmol/kg, and their comparison with reconstructions has been discussed previously (Köhler & Munhoven, 2020b). The simplistic structure of the model allows to resolve the effect of depth-dependent solubility on CSH, and CO$_3^{2-}$ concentrations were constant at depths below 1,000 m.

The long-term trends of CSH, CO$_3^{2-}$ and the marine carbon cycle are summarized for selected scenarios in Figure 2. The G/IG amplitudes in both variables were smaller earlier in the simulation than in the later part of the simulated Pleistocene. A North Atlantic stack in CO$_3^{2-}$ saturation (Sosdian, Rosenthal, & Toggweiler, 2018) from core sites below 2 km water depth located between 40 and 50°N, however, seems to be more comparable with the simulated CO$_3^{2-}$ in the surface Atlantic (Figure 2a) with G/IG amplitudes of up to 50 μmol/kg. Furthermore, the Atlantic data contain a long-term trend of 20 μmol/kg over the last 1.5 Ma, which is the opposite of what the results showed and also of what would be expected from multi-million-years changes in the carbonate chemistry (Zeebe & Tyrrell, 2019). This suggests that the composite in Sosdian, Rosenthal, and Toggweiler (2018) might not record Atlantic-wide changes in CO$_3^{2-}$ in deep waters. Chalk et al. (2019) who analyzed CO$_3^{2-}$ over the last 130 ka from similar locations, found that depending on Atlantic Ocean circulation regime the core sites are bathed in different water masses. Such water mass dependency is not contained in my box model results which complicates this data/model comparison further. Interestingly, a 500-ka long reconstruction of CO$_3^{2-}$ saturation in the deep Pacific (Kerr et al., 2017) had G/IG amplitudes of 10–20 μmol/kg, which is in reasonable agreement with the deep Pacific simulation results (Figure 2b). Thus, whereas the absolute values of simulated CSH and CO$_3^{2-}$ might be questionable, the changes in both variables on G/IG timescale are in reasonable agreement with reconstructions (Chalk et al., 2019; Kerr et al., 2017; Sosdian, Rosenthal, & Toggweiler, 2018; Yu et al., 2013). This implies that process-based CaCO$_3$ accumulation and dissolution in the sediments in the setup is meaningfully represented.
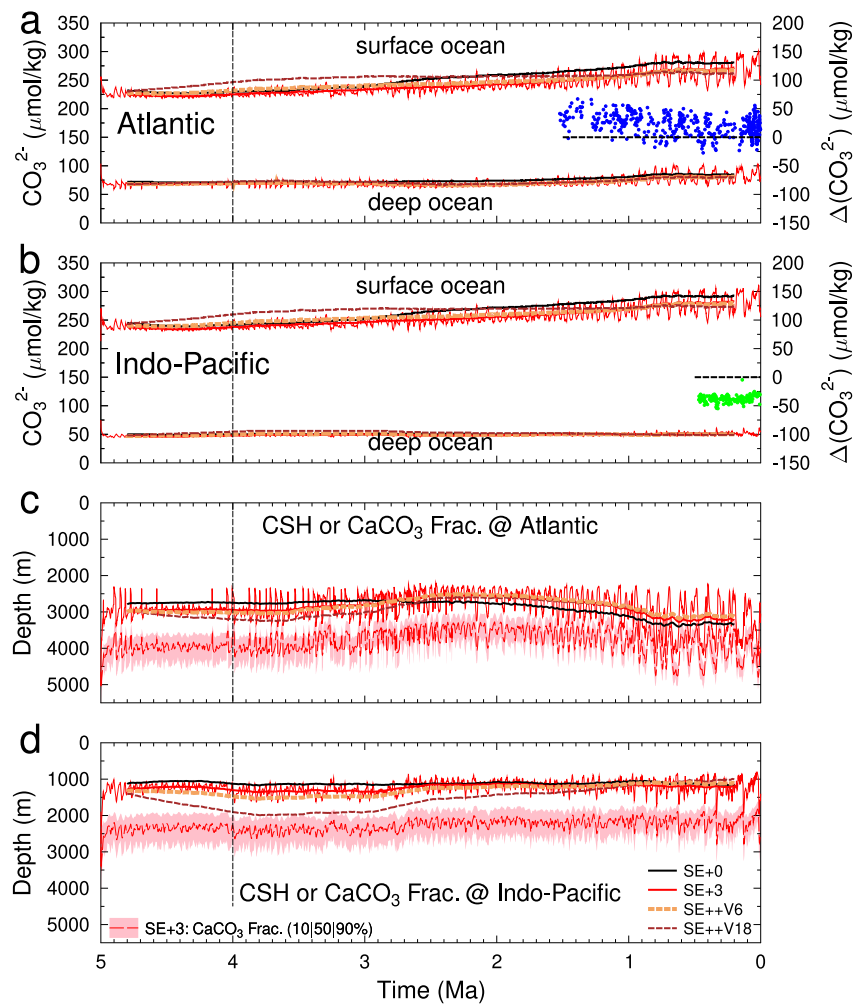
Figure 2. Simulated variables of the marine carbon cycle for selected scenarios. (a) Atlantic and (b) Indo-Pacific equatorial surface and deep ocean CO_3^{2-}-concentration. Calcite saturation horizons (CSH) in the water column as a function of water depth in (c) Atlantic and (d) Indo-Pacific. Long-term 400-ka running mean for all scenarios and underlying raw data for SE+3 are shown. Additionally, carbonate fraction (shaded area covers depths from 10% [lower bound] to 90% [upper bound] with 50% as broken line in between) as a function of water depth is plotted for scenario SE+3. Blue points in (a) are a composite of over/undersaturation of CO_3^{2-} in North Atlantic for the last 1.5 Ma (Sosdian, Rosenthal, & Toggweiler, 2018). Green points in (b) are deep Pacific undersaturation in CO_3^{2-} data (core TT013-PC72) (Kerr et al., 2017). Both data sets in (a, b) are plotted on individual y-axes (right) and the broken black lines mark the zero line in $\Delta(CO_3^{2-})$.

Furthermore, independent of the scenario, there is only a small long-term rise in deep ocean CO_3^{2-} of less than 10 (approximately 20) μmol/kg in the Indo-Pacific (Atlantic), while surface ocean CO_3^{2-} rose by approximately 50 μmol/kg over the last 4 Ma. Thus, the implicit assumption of a stable surface-to-deep ocean ratio in CO_3^{2-}, as made in other studies (Tyrrell & Zeebe, 2004; Zeebe & Tyrrell, 2019) was not supported by the simulations. The possibility that the calculated long-term rise in surface CO_3^{2-} from ~60 to 200 μmol/kg over the last 100 Ma in those studies may need a revision should be explored.

The temporal changes in the CSHs, which are water mass properties, mirrored the changes in the carbonate fraction in the sediments with the main difference being that the depth of the CSH was generally approximately 1 km above the 50% carbonate horizon in the sediments. This effect has been comprehensively discussed for the last 800 ka in Köhler and Munhoven (2020a), and is as an example shown for one scenario (Figures 2c and 2d). Most available reconstructions suggest that the carbonate compensation depth, typically the depth at which the carbonate fraction in the sediments is reduced to 10%, deepened by approximately 500 m in both the Atlantic and Indo-Pacific over the last 5 Ma (see compilation in Komar and Zeebe (2021)). While such long-term trends in the CSHs were also present in scenario SE+0 (Figures 2c and 2d), they seem to be opposite in scenarios with
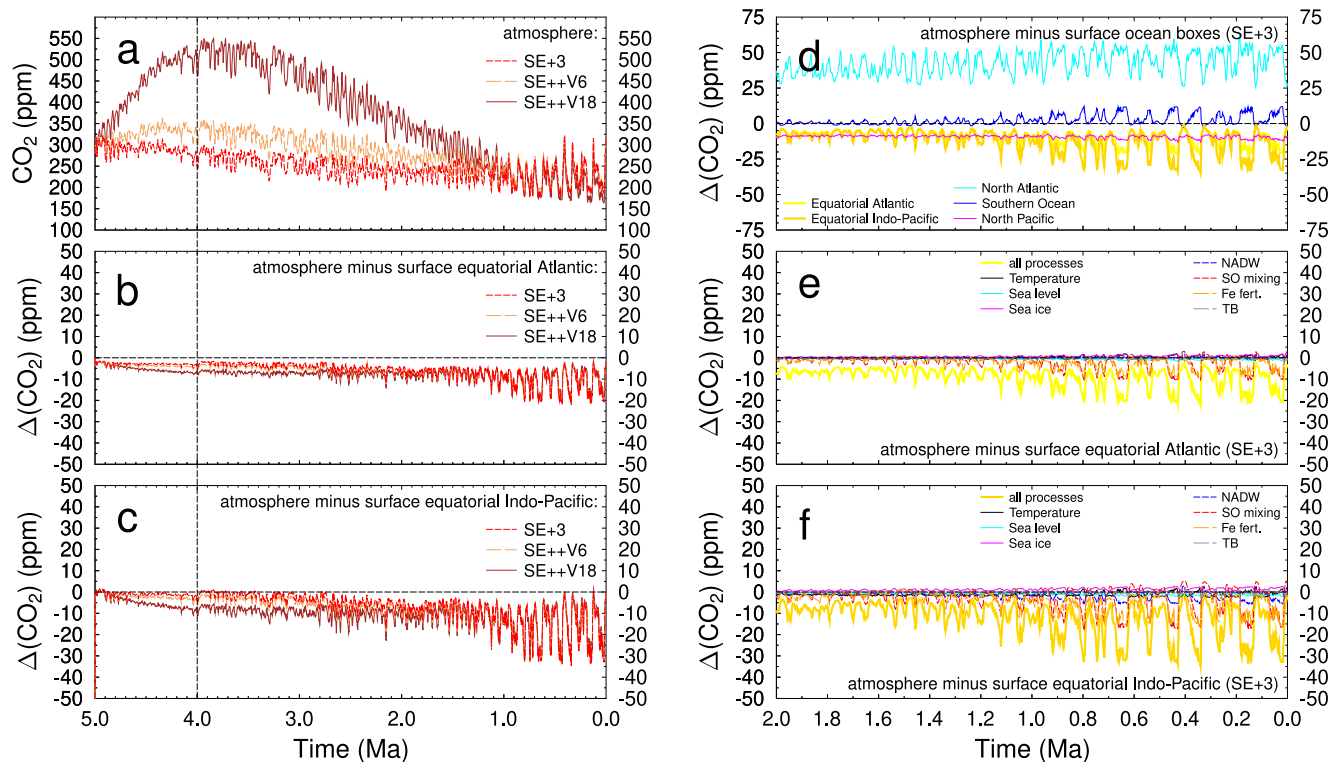
Figure 3. The difference between atmospheric CO_2 concentration and $p$$CO_2$ in surface waters. Atmospheric CO_2 concentration (a) and the difference to equatorial $p$$CO_2$ in surface waters (b: Atlantic; c: Indo-Pacific) for three selected scenarios (SE+3; SE++V6; SE++V18). (d–f): Zoom-in on the last 2 Ma for scenario SE+3 including contributions of indidivual processes to the differences in the equatorial boxes. (d) All surface ocean boxes; (e): equatorial Atlantic; (f): equatorial Indo-Pacific. The process of interest is switched off and the results subtracted from the control run with all processes active. The investigated processes are ocean temperature, sea level, sea ice, strength of the North Atlantic Deep Water (NADW) formation, vertical mixing in the Southern Ocean (SO), iron fertilization in the Southern Ocean, and changes in the terrestrial biosphere (TB).

a large long-term decline in volcanic CO_2 outgassing, for example, SE++V18, suggesting that this might be a rather unlikely scenario.

3.2. Is $p$$CO_2$ in Equatorial Surface Waters Always in Near-Equilibrium With the Atmosphere?

I next investigated whether the assumption of surface water equilibration with atmospheric $p$$CO_2$ was stationary in the locations of δ^{11}B generation. Plotting the anomaly in CO_2 concentration in the atmosphere and the equatorial surface waters of either the Atlantic or the Indo-Pacific (Figures 3b and 3c), I found for interglacial conditions that in both equatorial regions $p$$CO_2$ agreed within 5 ppm with the atmosphere. However, during glacial conditions simulated $p$$CO_2$ in the surface equatorial Atlantic box was up to 25 ppm higher than atmospheric CO_2 concentration independent of the simulation scenario and of the absolute values in atmospheric CO_2. In the Indo-Pacific this atmosphere-to-surface ocean disequilibrium in $p$$CO_2$ was up to 35 ppm during glacials. This offset is caused in the BICYCLE-SE model by the polar processes which contributed to the simulated glacial drawdown of CO_2 (Köhler & Munhoven, 2020b) effectively resulting in a depletion of CO_2 in the North Atlantic and Southern Ocean surface waters with respect to atmospheric CO_2, while equatorial regions are enriched (Figure 3d). While an enhanced solubility pump due to colder glacial temperatures contributes up to 30 ppm to the glacial CO_2 drawdown, this process has hardly any effect on the glacial disequilibrium. Contributing to the glacial CO_2 drawdown in polar regions are glacial iron fertilization and reduced glacial vertical mixing both in the Southern Ocean, but to some extent also a reduced glacial AMOC. Each process is responsible for up to 15 ppm of the simulated glacial disequilibrium between atmosphere and equatorial surface ocean (Figures 3e and 3f). The importance of polar processes for glacial CO_2 drawdown has also been proposed by other models (e.g., Bouttes et al., 2011; Menviel et al., 2017).

Notably, in the δ^{11}B-based CO_2 reconstructions that overlap with the ice core record, such a glacial disequilibrium is not easily detectable because assumptions made for the second variable of the marine carbonate system

might counteract its effect, for example, by assuming too small G/IG amplitudes in TA and DIC, as seen below. However, reconstructions for the last 30 ka (Henehan et al., 2013) might also point toward a glacial disequilibrium. similar as the simulation results, while no such offset was contained in Hönisch et al. (2009), which covers the last 800 ka. The agreement of surface water $p\mathrm{CO_2}$ derived from data of ODP 999 in the equatorial Atlantic with atmospheric $\mathrm{CO_2}$ from ice cores for the last glacial cycle, which are given as evidence for an unchanged equilibrium in Martínez-Botí et al. (2015) might therefore be questionable. However, note that in some studies (e.g., Chalk et al., 2017) the assumed uncertainty in an otherwise constant second parameter of the carbonate system is larger than the G/IG amplitudes proposed here. This would imply that the subsequent effect of the second parameter on $p\mathrm{CO_2}$ would be embedded in its uncertainty bands. However, this is not identical to calculations based on assumed G/IG amplitudes in TA or DIC. Furthermore, if such effects are only contained in the uncertainties they might easily get neglected if only mean values are analyzed.

An ocean-only general circulation model driven by boundary conditions for the LGM (Völker & Köhler, 2013) suggests, that the disequilibrium here found might not be a model-specific result. In particular, for the locations of the cores in the West Pacific used in Guillermic et al. (2022) and of ODP 668 in the central Atlantic Völker and Köhler (2013) also found higher $\mathrm{CO_2}$ partial pressure in the surface waters than in the atmosphere, in agreement with glacial results presented here. However, the pattern of disequilibrium is spatially heterogeneous. For the location of ODP 999 close to Panama in the Caribbean Sea the model in Völker and Köhler (2013) might actually indicate the opposite, lower $p\mathrm{CO_2}$ in the surface waters than in the atmosphere. These ocean models are known to have problems in correctly simulating areas close to the coast, asking for caution in interpreting the later results. Also note, that in Völker and Köhler (2013) the focus was on ocean physics and not on the simulated glacial carbon cycle, which featured only ~40 ppm glacial drawdown of atmospheric $\mathrm{CO_2}$ and apart from surface-boundary driven changes in ocean circulation polar processes have been not been specifically investigated. Thus, no glacial iron fertilization or deep water production changes related to brine rejection in Southern Ocean have been envisaged here as done, for example, in Bouttes et al. (2011). Other Earth system models which simulate a glacial carbon cycle rarely plot spatially resolved air-sea $\mathrm{CO_2}$ disequilibrium (e.g., Menviel et al., 2017), thus preventing a wider model-based analysis of this feature. However, additional analysis of a glacial state obtained with the Community Earth System Model (Kurahashi-Nakamura et al., 2022) support what has already been found in Völker and Köhler (2013). A $\mathrm{CO_2}$ disequilibrium between surface ocean and atmosphere has also been reconstructed at 14 different globally distributed sites across Termination 1 (partly going as far back as 30 ka) with the aim to identify water masses which release $\mathrm{CO_2}$ to the atmosphere (Shuttleworth et al., 2021), indicating that a glacial disequilibrium is not an uncommon feature.

In summary, since different models agree in two of three areas in a suggested glacial disequilibrium it might be a robust feature, but higher resolved model applications might be necessary, and the explicit investigation of polar processes, for further support for a glacial disequilibrium around ODP999. Furthermore, if this glacial disequilibrium is real, a good fit of $\delta^{11}\mathrm{B}$-based $\mathrm{CO_2}$ reconstructions with ice core data for glacial times might arise from other biases in the system, for example, for not perfect assumptions on the second parameter of the marine carbonate system.

3.3. Carbonate Chemistry in Equatorial Surface Waters

The surface ocean $p\mathrm{H}$ is reconstructed using species-specific calibrations from $\delta^{11}\mathrm{B}$. Further changes in the environmental conditions are typically extracted from other measurements (e.g., SST from Mg/Ca, sometimes salinity from $\delta^{18}\mathrm{O}$). However, the crucial step for the calculation of atmospheric $\mathrm{CO_2}$ concentration is the chosen assumption on a second variable of the marine carbonate system, which is either TA or DIC. Here, I compiled all available data that have been published together with the original studies, revised in most recent data compilations (de la Vega et al., 2020; Dyez et al., 2018; Guillermic et al., 2022), or were available online from the paleo-co2.org database (Hönisch, 2021). I plotted the most recent version of a data set, that is, the data originally published in Hönisch et al. (2009), Bartoli et al. (2011), Chalk et al. (2017), Seki et al. (2010), Foster (2008), Henehan et al. (2013) as compiled in Dyez et al. (2018) and those of Martínez-Botí et al. (2015) as contained in de la Vega et al. (2020). I took all data as they were available online. Also note, that data in paleo-co2.org have not been post-processed or harmonized.

All available data and the internally consistent simulation results related to the $\delta^{11}\mathrm{B}$-based $\mathrm{CO_2}$ proxy are compiled for the equatorial Atlantic in Figure 4. A similar compilation for the Pacific based on a recent study (Guillermic et al., 2022) is found in Figure S7 in Supporting Information S1, while similar results for the Atlantic

based on the alternative temperature forcing are found in Figure S8 in Supporting Information S1. I primarily distinguished between on which species the δ^{11}B data have been measured (either *T. sacculifer* or *G. ruber*) but did not discriminate if data were derived from different cores (ODP 668 or 999, both situated in the equatorial Atlantic, or ODP 806 and 807 in the equatorial Pacific) because this was of secondary importance. However, data initially published in Seki et al. (2010) are marked with different symbols in Figure 4, since this is the only data set from the Atlantic with reconstructed CO_2 in the Pliocene above 500 ppm, while other studies (de la Vega et al., 2020; Martínez-Botí et al., 2015) come to smaller numbers. The time series of δ^{11}B (Figure 4a) already had a species-specific signature: δ^{11}B based on *G. ruber* generally had lower values than δ^{11}B based on *T. sacculifer*. These δ^{11}B differences are well known and are partly related to the measurement techniques applied. Negative thermal ion mass spectrometry measures higher δ^{11}B values for the same sample than multi-collector inductively coupled plasma mass spectrometry (MC-ICP-MS). Most *T. sacculifer* data in this Atlantic compilation were measured by Negative thermal ion mass spectrometry, and all *G. ruber* data and eight *T. sacculifer* data were measured using MC-ICP-MS. When measured with the same technique, *G. ruber* gave ∼1‰ higher values than *T. sacculifer*. The differences in measurements obtained using the different techniques were consistent and were included in the calibrations applied for each analytical technique and foraminifera species (de la Vega et al., 2020; Farmer et al., 2016; Foster et al., 2013; Hönisch et al., 2019a). The Pacific data were all measured with MC-ICP-MS and no apparent species-specific offset in δ^{11}B is contained (Figure S7a in Supporting Information S1). More on these species-specific and technique-specific corrections to be applied on the measured δ^{11}B and how to derive *p*H is found in the related papers that describe the measurements.

Some of the technique- or species-specific offsets were reduced once δ^{11}B was transferred into *p*H (Figure 4b); however, there was still no universal agreement on the evolution of the equatorial surface Atlantic *p*H, and values based on different species or techniques did not always agree within their uncertainties. The G/IG changes in *p*H of 0.1–0.2 during the last 2 Ma generally agreed with the simulation results and reconstructions. For earlier times, the simulated *p*H became more a function of the assumed scenario with smaller G/IG amplitudes and a gradual long-term increase by 0.1–0.2. This smaller G/IG amplitude before 2 Ma was only contained in *T. sacculifer*-based *p*H to some extent and was lacking in *G. ruber*-based *p*H (Figure 4b). Furthermore, while the different scenarios spanned a wide range of possible *p*H variations, they still failed to capture the range span by the reconstructions. For example, between 3.0 and 3.5 Ma *T. sacculifer* and *G. ruber* spanned the ranges 8.05–8.2 and 7.9–8.1, respectively, while the simulation scenarios lay between 8.0 and 8.2. The G/IG amplitudes in *p*H before 2 Ma in the simulations were likely too small and were connected with similarly small G/IG amplitudes in other variables, for example, ocean δ^{13}C (Figure S4 in Supporting Information S1). They might be improved by further refinement of the Southern Ocean vertical mixing. The long-term disagreement in the range of simulated and reconstructed data favored neither *T. sacculifer*- or *G. ruber*-based reconstructions.

SST and salinity reconstructions had rather high uncertainties and generally corresponded within their error margins with the climate forcing that drove the simulations (Figures 4c and 4d). The data from de la Vega et al. (2020), which also revised the data previously published in Martínez-Botí et al. (2015), assumed a salinity of 35 ± 1.5 psu (1σ) between 2 and 4 Ma clearly fell lower than what others assumed or the simulation forcing suggested, but still overlapped within error margins. A constant salinity level, an assumption made sometimes, is clearly a simplification that neglects G/IG ice sheet growth and decay, although the range of this variability is typically contained in the assumed uncertainty. However, salinity has a minor effect on *p*H and *p*CO_2 calculations (Hönisch et al., 2019a; Hönisch & Hemming, 2005). For example, an increase in salinity by 1 PSU with everything else being equal would lead in offline calculations to an increase in atmospheric CO_2 concentration in the order of 5–10 ppm (Zeebe & Wolf-Gladrow, 2001).

When TA is taken as the second variable of the marine carbonate system, its changes have often (e.g., Dyez et al., 2018) been calculated as a function of salinity (Figure 4e). This approach only includes the effect of sea level variations (if they are contained in the assumed salinity variations) on any oceanic tracer concentration, which is on G/IG timescale of the order of 3%. Before 1.5 Ma the assumed TA varied only slightly, if at all. Other approaches are more specific. Chalk et al. (2017) changed TA as function of *p*H and tested its importance when compared to a constant value. In the data set from the Pacific different scenarios for TA have been tested, and the finally chosen TA time series is based on a study on weathering (Caves et al., 2016) and contains a long-term rise in TA by 200 µmol/kg over the last 5 Ma, approximately in agreement with the scenario SE+3, which contained no long-term trend in volcanic CO_2 outgassing (Figure S7e in Supporting Information S1). However, the simulation results clearly show that TA in both equatorial surface regions has a G/IG amplitude on the order
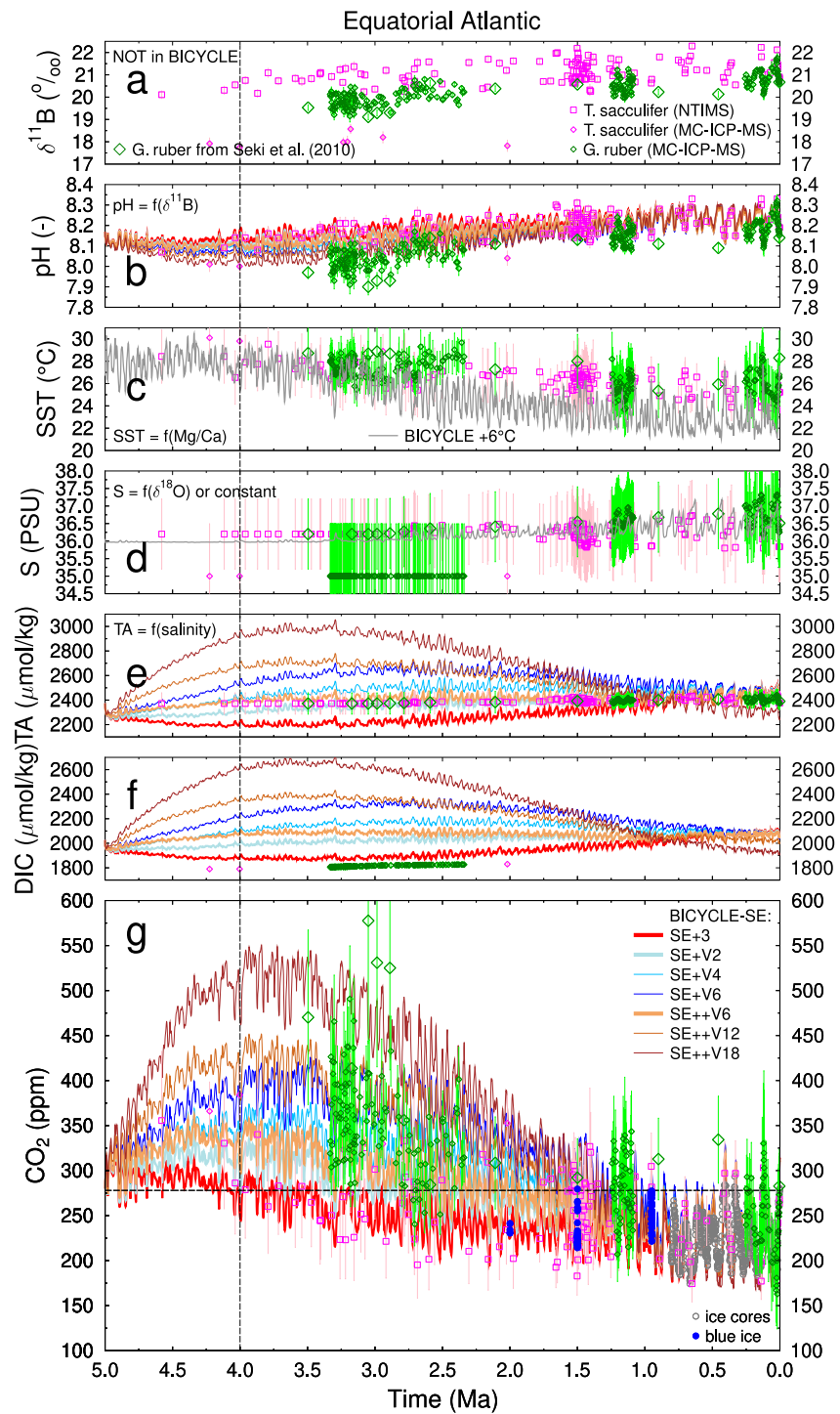
Figure 4. Details on the δ^{11}B-based CO$_2$ proxies from the surface equatorial Atlantic (see legends in subfigures a and g): (a) measured δ^{11}B; (b) pH; (c) sea surface temperature; (d) salinity; (e) TA; (f) DIC; (g) atmospheric CO$_2$. Data as compiled in Dyez et al. (2018) with updates from de la Vega et al. (2020) and paleo-co2.org with additions of CO$_2$ from ice cores (Bereiter et al., 2015) and blue ice (Yan et al., 2019). As 2nd variable of the carbonate system nearly all studies estimates TA, while de la Vega et al. (2020) estimates dissolved inorganic carbon. Data originally published in Seki et al. (2010) are marked with different symbols, since they contain the unusual high CO$_2$ values around 3 Ma. All uncertainties are ±1σ.

of 100 μmol/kg with glacials having higher values than interglacials. Slightly more than half of this G/IG amplitude was caused by reduced glacial sea level, while the rest is a result of the complex ocean-sediment interactions related to the carbonate compensation feedback, as described in detail in Köhler and Munhoven (2020a). In an exemplary setting similar to the surface equatorial Atlantic (TA: 2,300–2,500 μmol/kg, DIC: 2,000 μmol/kg, SST: 25°C, S: 36 PSU) such a G/IG change in TA of 100 μmol/kg — with all else being equal — would lead in offline calculations to CO_2 changes on the order of 100 ppm (Zeebe & Wolf-Gladrow, 2001). Furthermore, the assumed weathering strength and volcanism influence long-term trends in TA, which at 3 Ma was scenario-dependent between 2,200 and 3,000 μmol/kg (Figure 4e). Interestingly, scenario SE+3 (without any long-term change in volcanism) was the one with the lowest TA before 1 Ma and showed a long-term rise in TA. Long-term stable TA might only be obtained with a gradual decline in volcanic CO_2, as in scenario SE+V2.

There is only one Plio-Pleistocene study (de la Vega et al., 2020), which used DIC as the second variable of the marine carbonate system (Figure 4f). Here, DIC was taken from Sosdian, Greenop, et al. (2018), wherein it was calculated out of reconstructed deep ocean CO_3^{2-} ending in a DIC of ~1,800 μmol/kg around 3 Ma at the lower end of the simulated range that extends up 2,600 μmol/kg. The results of Sosdian, Greenop, et al. (2018) agreed roughly with the scenario SE+3 (no long-term trend in volcanism), but even within their stated uncertainties, it does not capture the G/IG amplitudes of ~50 μmol/kg in the simulations. Furthermore, as discussed above, a comparison of the simulated and reconstructed ocean $\delta^{13}C$ (Figure S4 in Supporting Information S1) suggests that the simulated G/IG amplitudes in most variables of the carbon cycle in the earlier parts of my simulations are potentially too small. This implies that assumed G/IG amplitudes in DIC in de la Vega et al. (2020) are smaller than the simulated amplitudes obtained here.

The wide ranges in simulated DIC or TA for the different scenarios follow the necessity to cover the range of atmospheric CO_2 found in the reconstructions. These ranges shrink already by more than 200 μmol/kg each, if the most extreme scenario SE++V18 (strong CO_2-dependency in weathering fluxes and a 18% long-term decline in volcanic CO_2 outgassing between 4.5 and 1 Ma) with atmospheric CO_2 above 500 ppm is avoided, for which some arguments are given in Section 3.4.

The resulting atmospheric CO_2 concentration, as stated in the $\delta^{11}B$-based reconstructions and from the simulations, generally spans the range from 300 to 500 ppm in the mid-Pliocene, with three points based on Atlantic data showing even higher values (Figure 4g). Interestingly, these three points are recalculations made in Dyez et al. (2018) from data originally published in Seki et al. (2010), in which finally calculated CO_2 values have been below 500 ppm. Although the underlying $\delta^{11}B$ values to these points are at the lower range of measurements (Figure 4a), it seems that especially the second variable of the carbonate system differently chosen in Dyez et al. (2018) is mainly responsible for these high CO_2 values. Data from the Pacific are in the Pliocene on average higher than those from the Atlantic with reconstructed concentration as high as 600 ppm (Figure 1a, Figure S7g in Supporting Information S1). Note that different simulation scenarios were designed to capture the range in the CO_2 reconstructions based on Atlantic data. Without further information, for example, CO_2 concentration from other sources or more reconstructions of other variables of the carbon cycle, it is not possible to decide on a most likely scenario. However, note that *G. ruber*-based data from approximately 3 Ma (de la Vega et al., 2020), which generally agreed with DIC from scenario SE+3, contain an atmospheric CO_2 of more than 400 ppm, while the simulated CO_2 in that scenario remained below 300 ppm. Up to 25 ppm of this gap might be explained during glacial times by the disequilibrium between the atmosphere and the surface of the equatorial Atlantic. The rest has its root in the difference in *p*H, with SE+3 having the highest *p*H in the range of plotted scenarios, whereas *p*H in de la Vega et al. (2020) would be more in line with other scenarios with long-term trends in volcanic outgassing. Thus, the *p*H and DIC in de la Vega et al. (2020) disagree with the internally consistent carbon cycle of the model, which should contain the possible relationships of the different variables of the marine carbonate system (here *p*H and DIC) based on the given boundary conditions. Similarly, in the Pacific data (Guillermic et al., 2022) the assumed TA agrees with the scenario SE+3, but the reconstructed *p*H are for most data points lower than the most extreme scenario SE++V18 (Figure S7 in Supporting Information S1). Thus, the carbonate system in Guillermic et al. (2022) seems also to contain a relationship between TA and *p*H that disagrees with what the internally consistent carbon cycle of the model allows to be possible.

Reconstructed *p*H in Atlantic and Pacific agreed with each other for the late Pleistocene, as also seen in modern data (Jiang et al., 2019), but diverged for the Pliocene with $\delta^{11}B$ values which are lower in the Pacific than in the Atlantic (Figure 1c). Such a difference in Pliocene equatorial surface water *p*H between Atlantic and Pacific is not contained in the model. Furthermore, present day data and future projections of surface ocean *p*H (Jiang
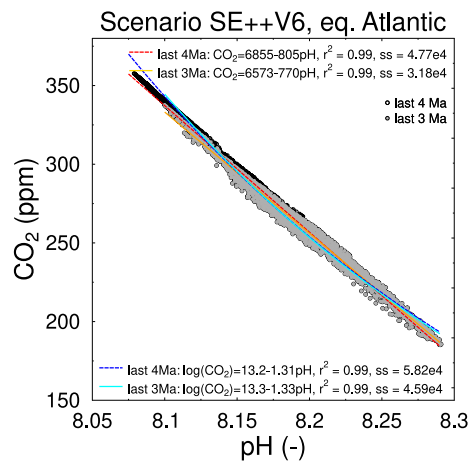
Figure 5. Example of a linear regression plot between atmospheric CO_2 and pH in the surface equatorial Atlantic for scenario SE++V6. In the lower left corner the calculated regression functions are given, if, as suggested (Hain, Foster, & Chalk, 2018) the logarithm of atmospheric CO_2 is calculated as function of surface equatorial Atlantic pH. ss is the calculated sum of squares, which here indicates that the linear fit performs better than the logarithmic fit.

et al., 2019) suggest that surface pH in both ocean basins should evolve similar for rising atmospheric CO_2 concentration. This should also be the case for the Pliocene unless ocean circulation has been structurally much different from that in future projections for which little evidences exist so far (e.g., Haywood et al., 2020; Zhang et al., 2021). This suggests that the pH reconstructions in the Pliocene might be problematic for unknown reasons. Pacific pH in the most recent study (Guillermic et al., 2022) is outside of the range given by multiple Atlantic studies (de la Vega et al., 2020; Dyez et al., 2018) in the Pliocene.

It should be emphasized that although the details of the model results might be biased (e.g., they are based on the applied forcing and partly dependent on the chosen box model geometry) the internally consistent carbon cycle builds upon knowledge of how temperature and salinity influence parameters of marine carbonate chemistry (Mojica Prieto & Millero, 2002; Zeebe & Wolf-Gladrow, 2001). The alternative temperature forcing based on Stap et al. (2018a), for example, leads to in principle similar results, but with smaller G/IG amplitudes in all variables (see equatorial Atlantic results for comparison in Figure S8 in Supporting Information S1). Thus, the described differences in the assumptions made for the carbonate system in understanding of the δ^{11}B-based CO_2 proxy with my simulation output (pH and DIC in de la Vega et al. (2020) and pH and TA in Guillermic et al. (2022)) might point to areas where further improvements are necessary.

3.4. Further Model-Based Insights on δ^{11}B-Based CO_2 Reconstructions

With the available information, potential disagreements in the carbon cycle can be highlighted, but it is still not possible to reliably choose which of the simulation scenarios might be most plausible. However, the modeling framework can be used to generate further consistency checks and insights to support δ^{11}B-based reconstructions. To this end, the relationships between various variables of the marine carbonate system were analyzed. It was found that simulated atmospheric CO_2 concentration was highly linearly related to pH in the surface waters of the equatorial Atlantic with $r^2 > 0.9$, sometimes as high as $r^2 = 1.00$ (Figure 5, Figures S9 and S10 in Supporting Information S1). Similar good linear fits are obtained between atmospheric CO_2 concentration and pH from the surface equatorial Indo-Pacific (Figure S11 in Supporting Information S1). Interestingly, the linear relationships between pH and TA or pH and DIC in the surface waters of the equatorial Atlantic (Figure S10 in Supporting Information S1) were not only weaker than for pH and CO_2, they also reversed to an anti-correlation in scenarios with high volcanic CO_2 emission and strong weathering feedback (SE++V18). Here, the long-term solid Earth influences were superimposed (and dominated the overall relation) on the still existing G/IG variability. No such reversal as function of scenario is found between pH and CO_2 making this also the more robust relationship. It has been found analytically (Hain, Foster, & Chalk, 2018) that changes in $\log_{10}(CO_2)$ are linearly and inversely related to changes in pH, where CO_2 is the concentration of dissolved CO_2 in the surface water, in which pH is measured. This finding was based on the argument that changes in pH are much more important for CO_2 than changes in HCO_3^- or in two parameters of the carbonate system, pK_0 and pK_1. To further distinguish if linear or logarithmic equations better fit to the simulation results in these scatter plots I also report the sum of squares (ss) which is a measure of the error of the regression, with a smaller ss pointing to the preferable regression equation. Here, $ss = \sum_{i=1}^{n}(y_i - y_{i,r})^2$, with i running over all data points $n = 3{,}001$ (3 Ma) or $n = 4{,}001$ (4 Ma) that are analyzed in steps of 1 ka. y_i is the simulated variable to the corresponding x_i, and $y_{i,r}$ the calculated variable following either a linear or $\log_{10}$ equation. These ss show that in my simulations the fit of $\log_{10}(CO_2)$ against pH becomes better than the linear fit of CO_2 against pH whenever CO_2 partial pressure in the equatorial surface waters is fitted against pH (right panels in Figures S9 and S11 in Supporting Information S1), bringing model-based confirmation to this theoretically derived relationship between both variables (Hain, Foster, & Chalk, 2018). However, if atmospheric CO_2 is fitted against pH the linear regression has smaller ss than a logarithmic equation (left panels in Figures S9 and S11 in Supporting Information S1) and should be preferred in all but the most extreme case (scenario SE++V18), which has in Section 3.1 already been classified as a rather unlikely scenario due deep ocean offsets.

These nearly perfect fits between pH and atmospheric CO_2 concentration support the earlier suggestion (Hain, Foster, & Chalk, 2018) that instead of making rather uncertain assumptions on a second variable of the marine carbonate system to determine atmospheric pCO_2, these calculations might be done relying entirely on pH. However, because the slope of these linear fits depends on the chosen simulation scenario, I can still only make suggestions about how CO_2 concentration as a function of pH might vary. For the final CO_2 values, one still has to make an educated choice in the scenario. With all available information combined, including carbonate compensation depth (Figure 2), the best guess scenarios are those with a gradual decreasing trend in volcanic CO_2 outgassing, namely SE+V2 or SE++V6, which are both marked by bold lines in Figure 4g. These scenarios reach nearly identical CO_2 concentration with maximum interglacial values at 3.5 Ma of approximately 350 ppm. Simulated CO_2 and CO_2 calculated out of pH in that way disagree in these best guess scenarios by less than 20 ppm, most of the time, and sometimes by less than 10 ppm (Figure S9 in Supporting Information S1). Such close fits reflect the relationship between pH and CO_2 that emerges from the model. However, because it is unknown how far from the truth the model results are, they should not be used directly for δ^{11}B-based CO_2 calculations, but as a consistency check instead.

Using the obtained fit from the selected scenario SE++V6, CO_2 is recalculated directly from δ^{11}B-based pH (Figure 6, Figures S12 and S13 in Supporting Information S1). The fit had an r^2 of 0.99 and may slightly underestimate the full interglacial values for the lowest pH below 8.1 (Figure 5). The calculated late Pleistocene CO_2 concentration with unrealistically low values of approximately 150 ppm (Figure 6c) were thus already embedded in the high glacial pH reconstructions of $\sim$8.3 (Figure 4b). Three of the *G. ruber*-based values approximately 3.5–3.0 Ma—all based on data initially published in Seki et al. (2010) and recalculated by Dyez et al. (2018)—are reduced by 50–100 ppm when based on the recalculation, suggesting that the original stated high values of 500–600 ppm are inconsistent with all knowledge of the carbon cycle that went into the equations of the BICYCLE-SE model. I also calculate CO_2 uncertainties in the approach based pH which are only based on the uncertainties in the reconstructed pH and how they transfer with the obtained fitting function into uncertainties in CO_2 under the assumption of a perfect fit motivated by the high r^2, although this approach might underestimate structural uncertainties. In the original studies the final CO_2 uncertainties are based on both uncertainties in pH and in the second parameter of the carbonate system. By this approach CO_2 uncertainties were generally reduced by about 30 ppm, in a few individual cases by up to 100 ppm (Figure 6b). The differences in the mean values between the original proposed CO_2 and my pH-based calculations were highly scenario-dependent (Figure 6a, Figures S11a and S11c in Supporting Information S1), and the scatter plots of CO_2 against pH (Figure 5, Figure S9 in Supporting Information S1) indicate the location of weak individual fits.

For data from the Pacific (Figure S13 in Supporting Information S1) the picture is more diverse. Before 2.5 Ma the calculated CO_2 concentration based solely on pH contained up to 100 ppm smaller uncertainties than the reconstructions, while for the more recent periods the calculated uncertainties were also increased with respect to the reconstructions by up to 30 ppm. The reconstructed high CO_2 concentrations of up to 600 ppm are in the recalculations not in general reduced, as has been the case for the high CO_2 values based on data from the Atlantic. This implies, that these high values are not caused by an inconsistent carbonate system (but remember that assumed TA and reconstructed pH were not combined in a similar way in any of the simulation scenarios), but that they are already embedded in the reconstructed pH values. However, I reiterate that all the model simulations were unable to reach as low values in pH in the surface equatorial Indo-Pacific as suggested in Guillermic et al. (2022). Going one step further one sees that the δ^{11}B in the Pacific is subdivided with values below $\sim$17‰ before 3 Ma, and above thereafter (Figure S7a in Supporting Information S1), a dynamic not seen in the Atlantic (Figure 4a). The reason for this difference is yet unknown, but it might be connected with the species-specific fractionation since there is also a change in the used foraminifera species at that point in time with *T. sacculier* being soley used before 3 Ma.

Note, that for the performed linear regression analysis one assumption is that the underlying variables should be independent from each other. Although global processes influence atmospheric CO_2 differently than surface ocean pH, this assumption is not always strictly fulfilled. The marine carbonate system has two degrees of freedom, but the nearly perfect fits indicate that further simplification seems possible.
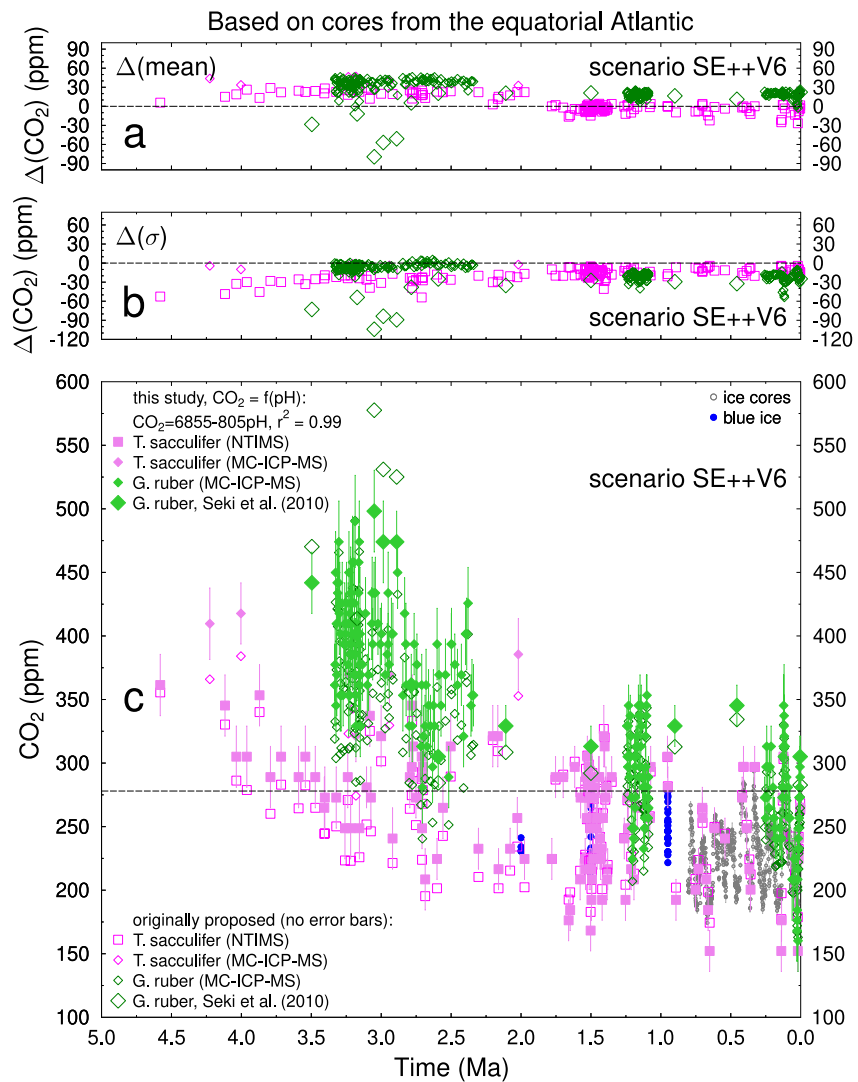
Figure 6. Calculating atmospheric CO_2 out of $\delta^{11}B$-based pH using linear regressions for scenario SE++V6 based on core sites in the equatorial Atlantic (de la Vega et al., 2020; Dyez et al., 2018). Data originally published in Seki et al. (2010) are marked with different symbols, since they contain the unusual high CO_2 values around 3 Ma. Changes in the mean values (a) and of the uncertainties (b), and comparing original proposed and newly calculated atmospheric CO_2 (c) with additions of CO_2 from ice cores (Bereiter et al., 2015) and blue ice (Yan et al., 2019). I use the linear regressions between pH and CO_2 as obtained from 4 Ma data. The differences are always plotted as new calculated values minus originally reconstructed values.

4. Discussion

While the applied forcing is fully responsible for how the model simulates changes in the carbon cycle in detail, the intrinsic relationships between different variables of the marine carbonate system are independent of it. For example, the detailed distribution of DIC into HCO_3^-, CO_3^{2-}, and CO_2 is a function of temperature, salinity, and pressure, but changes in these climate variables will never lead to chemically unrealistic ratios between these three species of DIC. Even so, both TA and DIC in the surface layers of the ocean are responsible for how much CO_2 can be dissolved and is thus available for gas exchange with the atmosphere. This implies that the two alternative temperature forcings applied here, although both probably incorrect in detail, produce plausible carbon cycle changes, in which the relationships between the different variables of the marine carbonate system are nevertheless consistent. The consistency of the carbon cycle–climate system has even been taken a step further in Hain, Foster, and Chalk (2018) who showed that from only knowing the change in pH—potentially calculated from $\delta^{11}B$—one might be able to estimate the change in CO_2-based radiative forcing. Hain, Foster, and Chalk (2018) tested how temperature, or the addition or removal of either DIC or $CaCO_3$ influence the

CO_2-pH relationship and derived from these three different processes, that the slope of $\Delta \log_{10}(CO_2)/\Delta p$H falls in the range of about $-1.3{:}1$ and $-0.9{:}1$, which defined the uncertainty of their method. Here, I do not analyze individual processes, but simulations with an open system global carbon cycle model. I find, that the long-term slope between CO_2 and pH depends on the assumed scenario of volcanic CO_2 outgassing and weathering and cannot be tightly constrained without further knowledge. This difference to Hain, Foster, and Chalk (2018) might derive from the time-dependent weathering-related input of HCO_3^- into the ocean in my approach, which has not been checked for its to impact on CO_2 and pH in their study. However, they advice to use their approach only to time slices not longer than 1 million years due to the not covered long-term weathering dynamics, while I here analyzed 3–4 Ma long simulation results.

I tested the importance of the results on the chosen temperature forcing for two selected scenarios, the control run SE+3 and one of the most likely scenarios SE++V6 (Figure S14 in Supporting Information S1). The scenarios using the alternative temperature forcing of Stap et al. (2018a) (SE+3S, SE++V6S) led to similar equatorial surface ocean pH and atmospheric CO_2 containing similar linear relationships in their scatter plots, but for rather different DIC and TA inventories (Figure S14 in Supporting Information S1). These sensitivity experiments therefore highlight, that pH and atmospheric CO_2 are rather robust features of the simulations, while due to the two degrees of freedom in the marine carbonate system DIC and TA are individually weaker constrained, but due to geochemically possible changes in the global carbon cycle strongly link to each other. Actually, these offsets in TA and DIC between the setups with different temperature forcing make an educated guess on the value of a second variable of the marine carbonate system for the calculation of CO_2 out of pH in the boron-isotope CO_2 proxy even more challenging. The simulation results suggest that only the long-term relationship between CO_2 and surface ocean pH is a robust feature of the system.

Reconstructions of atmospheric CO_2 concentration based on alternative proxies, either alkenones in marine sediment cores or paleosols, do not yet improve our knowledge of past CO_2 due to other challenges. Paleosol-based CO_2 (Da et al., 2019) suggest in general the lowest values for the last 2.5 Ma, but the uncertainties with $1\sigma > 50$ ppm are very high. Alkenone-based approaches (Badger et al., 2013, 2019; Seki et al., 2010; Zhang et al., 2013) also suggest a wide range of possible CO_2 values across the Plio-Pleistocene, producing values lower than some of the δ^{11}B-based reconstructions, which generally remain below 400 ppm. This method uses the CO_2-dependent isotopic fractionation of carbon during photosynthesis (ε_p) and a physiological scaling parameter (b) that accounts for biological factors. However, it has been shown (Zhang et al., 2019) that b varies over glacial cycles, implying that CO_2 reconstructions based on a constant b are biased. Another study, although focusing on deeper times, suggests that the calibration of the alkenone-based approach requires a revision (Rae et al., 2021). Phelps et al. (2021) recently argued that the theory for the alkenone carbon isotope fractionation model is not supported by field data and should not be used to reconstruct past CO_2 changes before further studies successfully account for the effects of irradiance and cell size variations on isotopic fractionation. Furthermore, a recent review on carbon isotope fractionation in marine phytoplankton (Brandenburg et al., 2022) shows that ε_p can vary significantly between different phytoplankton species and groups, but also as a result of different culturing methods and differences in daylength. Based on these recent critiques I refrain from a further in-depth discussion of CO_2 reconstructions from alkenones.

Recently, Yamamoto et al. (2022) used leaf wax δ^{13}C as proxy for CO_2 extending back to 1.5 Ma. This approach has the advantage of directly inferring atmospheric CO_2, therefore circumventing the atmosphere-surface ocean disequilibrium problem. The fit of this proxy-based CO_2 to ice core CO_2 is $r^2 = 0.78$ making it a promising approach. Atmospheric CO_2 derived from leaf wax δ^{13}C and based on δ^{11}B agree in suggesting smaller G/IG amplitudes before the Mid Pleistocene Transition, but for different reasons (Figure 1a). Yamamoto et al. (2022) finds reduced interglacial CO_2 before the Mid Pleistocene Transition and hardly any changes in glacial values, while in Hönisch et al. (2009) and Chalk et al. (2017) interglacial CO_2 values stayed constant and glacial CO_2 have been higher earlier on. The data from Yamamoto et al. (2022) would still agree with the various scenarios presented in this study, but the time series is too short to use this information to prefer any of my volcanism/weathering scenarios. Therefore, I conclude that the alternative proxies cannot yet help in answering which of the different scenarios, with their different CO_2 values and different pH-CO_2-relationships, is the best choice.

Here, I used internally consistent carbon cycle knowledge derived from a global model transiently applied over the last 4 Ma and was thus able to apply consistency checks to the assumptions which went into the δ^{11}B-based CO_2 proxy. I found that the assumption of a near-equilibrium between the pCO_2 in the atmosphere and in the surface

equatorial ocean was only fulfilled in the simulations during interglacial climates (peak atmospheric pCO_2 during each glacial cycle), but both variables were offset in my model results by up to 25 ppm in the Atlantic and up to 35 ppm in the Indo-Pacific during glacials. This glacial disequilibrium is caused in the BICYCLE-SE model by the contribution of polar processes to the glacial CO_2 drawdown and is in two out of three site locations supported by other models, but needs further investigations around ODP999 in the Caribbean. If true, this glacial bias would complicate the assessment of the quality of any marine-based CO_2 reconstructions, since a good agreement with ice core CO_2 at glacial times would then imply a compensation from other biases. This is an upper quantification of the uncertainty of the atmosphere-surface ocean equilibrium assumption, which to my understanding was missing so far. Furthermore, the assumed values of a second variable of the marine carbonate system (TA or DIC) besides pH (itself calculated from $\delta^{11}B$) required to reconstruct CO_2 concentration were not always consistent with knowledge of carbon cycle changes as it was put into the model. This leads to some data points from the equatorial Atlantic at approximately 3.0–3.5 Ma from which a CO_2 concentration of ∼500–600 ppm was calculated, which in my internally consistent carbon cycle seemed to be 50–100 ppm too high. The underlying data of these high CO_2 values have been published in one of the earlier studies (Seki et al., 2010) and lab procedure and applied corrections might have improved since then leading to smaller Pliocene values in more recent studies (de la Vega et al., 2020). However, the main reason for these high CO_2 values seems to be the choices on the carbonate system made during recalculation within the compilation study of Dyez et al. (2018). Furthermore, G/IG amplitudes in TA, as suggested by the carbon cycle simulation studies discussed here, are seldom considered in $\delta^{11}B$-based reconstructions of CO_2. I acknowledge that assumed uncertainty ranges in TA in some cases might be large enough to cover these G/IG amplitudes, however, an assumed large uncertainty in TA still leads to different CO_2 reconstructions than assumed larger G/IG changes in mean TA. pH is for most reconstructions based on *G. ruber* from Atlantic cores and for most cases in the Pacific lower than what the carbon cycle model is able to simulate. Thus, the priority for future studies should be to further reduce this data/model mismatch in pH, because—as this study highlighted—pH alone seems to be most important for a meaningful reconstruction of atmospheric CO_2 concentration.

Independent and robust information on the long-term trends in volcanic CO_2 outgassing and on weathering strength, which are necessary to finally and with confidence favor a simulation scenario (and thus constrain CO_2) are not yet available. Associated changes in deep ocean CO_3^{2-}, and the carbonate compensation depth help to reduce the potential range of scenarios to the most likely ones, in which a gradual decline in volcanic outgassing is included. An even better fit to independent data might be obtained when using future compilations of temperature and sea level (Clark et al., 2021). My simulation results confirm the theoretically derived close relationship of $\log_{10}(CO_2)$ and pH, where CO_2 is the partial pressure in the equatorial surface water, in which also pH is measured (Hain, Foster, & Chalk, 2018). Thus, a fully global carbon cycle model supports the earlier theoretical proposal in that paper that it is possible to calculate atmospheric CO_2 concentration based on only one variable of the marine carbonate system (i.e., surface ocean pH). Because it is still unclear which of the proposed scenarios of volcanic CO_2 outgassing, weathering strength and their related atmospheric CO_2 are closest to reality it is not suggested to include model simulations in the calculation of the $\delta^{11}B$-based CO_2. However, the close linear relationship between atmospheric CO_2 and equatorial surface ocean pH found here might be used as test to help to identify if the assumptions made for the second variable of the carbonate system lead to plausible results, since their relationship is the most robust feature of the system, while due to the two degrees of freedoms in the marine carbonate chemistry both TA and DIC can vary widely. As a side product, the simulation results show that the surface-to-deep ocean ratio of CO_3^{2-} increased over time, in disagreement with some assumptions in other studies on multi-million-year trends in carbonate chemistry (Tyrrell & Zeebe, 2004; Zeebe & Tyrrell, 2019). Given the disagreement between variables of the marine carbonate system in the application of the $\delta^{11}B$-based CO_2 proxy and my internally consistent global carbon cycle simulations that have been identified here, I propose that models might help in improving the interpretation of this proxy in future applications.

Data Availability Statement

Data used here can be assessed as follows: (a) Forcing (input) data sets, simulation output, processed $\delta^{13}C$ data originally published in Poore et al. (2006); Lisiecki (2014), and additional SST data based on Stap et al. (2018a) are found in Köhler (2022). (b) Temperature forcing (Köhler et al., 2015a, 2015b). (c) Alternative temperature forcing (Stap et al., 2018a, 2018b). (d) Sea level forcing (de Boer et al., 2014, 2015). (e) Dust fluxes of the past 4 Ma, online supplement to Martinez-Garcia et al. (2011). (f) Deep Atlantic over/undersaturation in carbonate ion for the last 1.5 Ma, online supplement to Sosdian, Rosenthal, and Toggweiler (2018). (g) Deep

Pacific undersaturation in carbonate ion during the past five glacial cycles (Kerr et al., 2017, 2018). (h) Equatorial Atlantic carbonate chemistry and CO_2 data during the Mid-Piacenzian Warm Period: online supplement to de la Vega et al. (2020) and assuming a 1.5 PSU 1σ uncertainty of salinity as stated in the main text of that study. (i) Various sets of equatorial carbonate chemistry and atmospheric CO_2 data over the last 5 Ma: online supplement to Dyez et al. (2018). (j) Equatorial Pacific carbonate chemistry and CO_2 data during the last 5 Ma: online supplement to Guillermic et al. (2022). (k) Carbon fluxes from 800 ka simulations of BICYCLE-SE model (Köhler & Munhoven, 2020a, 2020b). (l) Carbonate chemistry data missing in above mentioned sources was taken from Hönisch (2021) without post-processing or harmonization. The BICYCLE-SE model is fully described in Köhler and Munhoven (2020b), and all changes performed for the study here are contained in the Methods section.

References

Badger, M. P. S., Chalk, T. B., Foster, G. L., Bown, P. R., Gibbs, S. J., Sexton, P. F., et al. (2019). Insensitivity of alkenone carbon isotopes to atmospheric CO_2 at low to moderate CO_2 levels. *Climate of the Past*, *15*(2), 539–554. https://doi.org/10.5194/cp-15-539-2019

Badger, M. P. S., Schmidt, D. N., Mackensen, A., & Pancost, R. D. (2013). High-resolution alkenone palaeobarometry indicates relatively stable pCO_2 during the Pliocene (3.3–2.8 Ma). *Philosophical Transactions of the Royal Society A: Mathematical, Physical & Engineering Sciences*, *371*(2001), 20130094. https://doi.org/10.1098/rsta.2013.0094

Bartoli, G., Hönisch, B., & Zeebe, R. E. (2011). Atmospheric CO_2 decline during the Pliocene intensification of northern hemisphere glaciations. *Paleoceanography*, *26*(4), PA4213. https://doi.org/10.1029/2010PA002055

Bereiter, B., Eggleston, S., Schmitt, J., Nehrbass-Ahles, C., Stocker, T. F., Fischer, H., et al. (2015). Revision of the EPICA Dome C CO_2 record from 800 to 600 kyr before present. *Geophysical Research Letters*, *42*(2), 542–549. https://doi.org/10.1002/2014GL061957

Berends, C. J., Köhler, P., Lourens, L. J., & van de Wal, R. S. W. (2021). On the cause of the Mid-Pleistocene Transition. *Reviews of Geophysics*, *59*(2), e2020RG000727. https://doi.org/10.1029/2020RG000727

Berner, R. A., Lasaga, A. C., & Garrels, R. M. (1983). The carbonate-silicate geochemical cycle and its effect on atmospheric carbon dioxide over the past 100 million years. *American Journal of Science*, *283*(7), 641–683. https://doi.org/10.2475/ajs.283.7.641

Börker, J., Hartmann, J., Amann, T., Romero-Mujalli, G., Moosdorf, N., & Jenkins, C. (2020). Chemical weathering of loess during the last glacial maximum, mid-Holocene and today. *Geochemistry, Geophysics, Geosystems*, *21*(7), e2020GC008922. https://doi.org/10.1029/2020GC008922

Bouttes, N., Paillard, D., Roche, D. M., Brovkin, V., & Bopp, L. (2011). Last glacial maximum CO_2 and $\delta^{13}C$ successfully reconciled. *Geophysical Research Letters*, *38*(2), L02705. https://doi.org/10.1029/2010GL044499

Brandenburg, K. M., Rost, B., de Waal, D. B. V., Hoins, M., & Sluijs, A. (2022). Physiological control on carbon fractionation in marine phytoplankton. *Biogeosciences*, *19*(13), 3305–3315. https://doi.org/10.5194/bg-19-3305-2022

Brovkin, V., Ganopolski, A., Archer, D., & Rahmstorf, S. (2007). Lowering of glacial atmospheric CO_2 in response to changes in oceanic circulation and marine biogeochemistry. *Paleoceanography*, *22*(4), PA4202. https://doi.org/10.1029/2006PA001380

Cavalieri, D. J., Gloersen, P., Parkinson, C. L., Comiso, J. C., & Zwally, H. J. (1997). Observed hemispheric asymmetry in global sea ice changes. *Science*, *278*(5340), 1104–1106. https://doi.org/10.1126/science.278.5340.1104

Caves, J. K., Jost, A. B., Lau, K. V., & Maher, K. (2016). Cenozoic carbon cycle imbalances and a variable weathering feedback. *Earth and Planetary Science Letters*, *450*, 152–163. https://doi.org/10.1016/j.epsl.2016.06.035

Chalk, T., Foster, G., & Wilson, P. (2019). Dynamic storage of glacial CO_2 in the Atlantic Ocean revealed by boron $[CO_3^{2-}]$ and pH records. *Earth and Planetary Science Letters*, *510*, 1–11. https://doi.org/10.1016/j.epsl.2018.12.022

Chalk, T. B., Hain, M. P., Foster, G. L., Rohling, E. J., Sexton, P. F., Badger, M. P. S., et al. (2017). Causes of ice age intensification across the Mid-Pleistocene Transition. *Proceedings of the National Academy of Sciences of United States of America*, *114*(50), 13114–13119. https://doi.org/10.1073/pnas.1702143114

Clark, P. U., Shakun, J. D., Rosenthal, Y., Köhler, P., Schrag, D. P., Pollard, D., et al. (2021). Requiem for the regolith hypothesis: Sea-level and temperature reconstructions provide a new template for the Middle Pleistocene Transition. *EGU General Assembly*, *2021*, EGU21–13981. online, 19–30 Apr 2021. https://doi.org/10.5194/egusphere-egu21-13981

Da, J., Zhang, Y. G., Li, G., Meng, X., & Ji, J. (2019). Low CO_2 levels of the entire Pleistocene epoch. *Nature Communications*, *10*(1), 4342. https://doi.org/10.1038/s41467-019-12357-5

de Boer, B., Lourens, L. J., & van de Wal, R. S. (2014). Persistent 400,000-year variability of Antarctic ice volume and the carbon cycle is revealed throughout the Plio-Pleistocene. *Nature Communications*, *5*(1), 2999. https://doi.org/10.1038/ncomms3999

de Boer, B., Lourens, L. J., & van de Wal, R. S. W. (2015). A 5 million year reconstruction of sea level, temperature, and sea water $\delta^{18}O$ [Dataset]. PANGAEA. https://doi.org/10.1594/PANGAEA.855850

de la Vega, E., Chalk, T. B., Wilson, P. A., Bysani, R. P., & Foster, G. L. (2020). Atmospheric CO_2 during the Mid-Piacenzian Warm Period and the M2 glaciation. *Scientific Reports*, *10*(1), 11002. https://doi.org/10.1038/s41598-020-67154-8

Dyez, K. A., Hönisch, B., & Schmidt, G. A. (2018). Early Pleistocene obliquity-scale pCO_2 variability at ~1.5 million years ago. *Paleoceanography and Paleoclimatology*, *33*(11), 1270–1291. https://doi.org/10.1029/2018PA003349

Evans, D., Brierley, C., Raymo, M. E., Erez, J., & Müller, W. (2016). Planktic foraminifera shell chemistry response to seawater chemistry: Pliocene-Pleistocene seawater Mg/Ca, temperature and sea level change. *Earth and Planetary Science Letters*, *438*, 139–148. https://doi.org/10.1016/j.epsl.2016.01.013

Farmer, J. R., Hönisch, B., & Uchikawa, J. (2016). Single laboratory comparison of MC-ICP-MS and N-TIMS boron isotope analyses in marine carbonates. *Chemical Geology*, *447*, 173–182. https://doi.org/10.1016/j.chemgeo.2016.11.008

Felis, T., Hinestrosa, G., Köhler, P., & Webster, J. M. (2022). Role of the deglacial buildup of the Great Barrier Reef for the global carbon cycle. *Geophysical Research Letters*, *49*(4), e2021GL096495. https://doi.org/10.1029/2021GL096495

Foster, G. L. (2008). Seawater pH, pCO_2 and $[CO_3^{2-}]$ variations in the Caribbean Sea over the last 130 kyr: A boron isotope and B/Ca study of planktic foraminifera. *Earth and Planetary Science Letters*, *271*(1–4), 254–266. https://doi.org/10.1016/j.epsl.2008.04.015

Foster, G. L., Hönisch, B., Paris, G., Dwyer, G. S., Rae, J. W., Elliott, T., et al. (2013). Interlaboratory comparison of boron isotope analyses of boric acid, seawater and marine $CaCO_3$ by MC-ICPMS and NTIMS. *Chemical Geology*, *358*, 1–14. https://doi.org/10.1016/j.chemgeo.2013.08.027

Ganachaud, A., & Wunsch, C. (2000). Improved estimates of global ocean circulation, heat transport and mixing from hydrographic data. *Nature*, *408*(6811), 453–457. https://doi.org/10.1038/35044048

Gersonde, R., Crosta, X., Abelmann, A., & Armand, L. (2005). Sea-surface temperature and sea ice distribution of the Southern Ocean at the EPILOG last glacial maximum—A circum-Antarctic view based on siliceous microfossil records. *Quaternary Science Reviews*, *24*(7–9), 869–896. https://doi.org/10.1016/j.quascirev.2004.07.015

Guillermic, M., Misra, S., Eagle, R., & Tripati, A. (2022). Atmospheric CO_2 estimates for the Miocene to Pleistocene based on foraminiferal $\delta^{11}B$ at ocean drilling program sites 806 and 807 in the Western Equatorial Pacific. *Climate of the Past*, *18*(2), 183–207. https://doi.org/10.5194/cp-18-183-2022

Haeberli, M., Baggenstos, D., Schmitt, J., Grimmer, M., Michel, A., Kellerhals, T., & Fischer, H. (2021). Snapshots of mean ocean temperature over the last 700000 years using noble gases in the EPICA Dome C ice core. *Climate of the Past*, *17*(2), 843–867. https://doi.org/10.5194/cp-17-843-2021

Hain, M. P., Foster, G. L., & Chalk, T. (2018). Robust constraints on past CO_2 climate forcing from the boron isotope proxy. *Paleoceanography and Paleoclimatology*, *33*(10), 1099–1115. https://doi.org/10.1029/2018PA003362

Hain, M. P., Sigman, D. M., Higgins, J. A., & Haug, G. H. (2015). The effects of secular calcium and magnesium concentration changes on the thermodynamics of seawater acid/base chemistry: Implications for Eocene and Cretaceous ocean carbon chemistry and buffering. *Global Biogeochemical Cycles*, *29*(5), 517–533. https://doi.org/10.1002/2014GB004986

Hain, M. P., Sigman, D. M., Higgins, J. A., & Haug, G. H. (2018). Response to comment by Zeebe and Tyrrell on *the Effects of secular Calcium and magnesium concentration Changes on the Thermodynamics of seawater acid/base chemistry: Implications for the Eocene and cretaceous ocean carbon Chemistry and buffering*. *Global Biogeochemical Cycles*, *32*(5), 898–901. https://doi.org/10.1002/2018GB005931

Hartmann, J., Jansen, N., Dürr, H. H., Kempe, S., & Köhler, P. (2009). Global CO_2-consumption by chemical weathering: What is the contribution of highly active weathering regions? *Global and Planetary Change*, *69*(4), 185–194. https://doi.org/10.1016/j.gloplacha.2009.07.007

Hartmann, J., Moosdorf, N., Lauerwald, R., Hinderer, M., & West, A. J. (2014). Global chemical weathering and associated P-release: The role of lithology, temperature and soil properties. *Chemical Geology*, *363*(0), 145–163. https://doi.org/10.1016/j.chemgeo.2013.10.025

Haywood, A. M., Dowsett, H. J., Dolan, A. M., Rowley, D., Abe-Ouchi, A., Otto-Bliesner, B., et al. (2016). The Pliocene model intercomparison project (PlioMIP) phase 2: Scientific objectives and experimental design. *Climate of the Past*, *12*(3), 663–675. https://doi.org/10.5194/cp-12-663-2016

Haywood, A. M., Tindall, J. C., Dowsett, H. J., Dolan, A. M., Foley, K. M., Hunter, S. J., et al. (2020). The Pliocene model intercomparison project phase 2: Large-scale climate features and climate sensitivity. *Climate of the Past*, *16*(6), 2095–2123. https://doi.org/10.5194/cp-16-2095-2020

Henehan, M. J., Rae, J. W., Foster, G. L., Erez, J., Prentice, K. C., Kucera, M., et al. (2013). Calibration of the boron isotope proxy in the planktonic foraminifera *Globigerinoides ruber* for use in palaeo-CO_2 reconstruction. *Earth and Planetary Science Letters*, *364*(0), 111–122. https://doi.org/10.1016/j.epsl.2012.12.029

Hönisch, B. (2021). Paleo-CO_2 data archive (Version 1) [Dataset]. NOAA. https://www1.ncdc.noaa.gov/pub/data/paleo/climate_forcing/trace_gases/Paleo-pCO2/ (Download of data: 12th May 2021).

Hönisch, B., Eggins, S. M., Haynes, L. L., Allen, K. A., Holland, K. D., & Lorbacher, K. (2019a). Boron concentration and isotope ratio analysis. In *Boron proxies in Paleoceanography and Paleoclimatology chapter 4* (pp. 165–223). John Wiley & Sons, Ltd. https://doi.org/10.1002/9781119010678.ch4

Hönisch, B., Eggins, S. M., Haynes, L. L., Allen, K. A., Holland, K. D., & Lorbacher, K. (2019b). Reconstructing paleo-acidity, pCO_2 and deep-ocean $[CO_3^{2-}]$. In *Boron proxies in Paleoceanography and Paleoclimatology chapter 3* (pp. 120–164). John Wiley & Sons, Ltd. https://doi.org/10.1002/9781119010678.ch3

Hönisch, B., & Hemming, N. G. (2005). Surface ocean pH response to variations in pCO_2 through two full glacial cycles. *Earth and Planetary Science Letters*, *236*(1–2), 305–314. https://doi.org/10.1016/j.epsl.2005.04.027

Hönisch, B., Hemming, N. G., Archer, D., Siddall, M., & McManus, J. F. (2009). Atmospheric carbon dioxide concentration across the Mid-Pleistocene Transition. *Science*, *324*(5934), 1551–1554. https://doi.org/10.1126/science.1171477

Jiang, L.-Q., Carter, B. R., Feely, R. A., Lauvset, S. K., & Olsen, A. (2019). Surface ocean pH and buffer capacity: Past, present and future. *Scientific Reports*, *9*(1), 18624. https://doi.org/10.1038/s41598-019-55039-4

Kerr, J., Rickaby, R., Yu, J., Elderfield, H., & Sadekov, A. Y. (2017). The effect of ocean alkalinity and carbon transfer on deep-sea carbonate ion concentration during the past five glacial cycles. *Earth and Planetary Science Letters*, *471*, 42–53. https://doi.org/10.1016/j.epsl.2017.04.042

Kerr, J., Rickaby, R. E. M., Yu, J., Elderfield, H., & Sadekov, A. Y. (2018). B/Ca ratios in benthic foraminifera, carbonate ion concentrations, stable isotopes and reconstructed past seafloor $CaCO_3$ concentrations for ODP Site 130-806 [Dataset]. PANGAEA. https://doi.org/10.1594/PANGAEA.892511

Knorr, G., Barker, S., Zhang, X., Lohmann, G., Gong, X., Gierz, P., et al. (2021). A salty deep ocean as a prerequisite for glacial termination. *Nature Geoscience*, *14*(12), 930–936. https://doi.org/10.1038/s41561-021-00857-3

Köhler, P. (2020). Anthropogenic CO_2 of high emission scenario compensated after 3500 years of ocean alkalinization with an annually constant dissolution of 5 Pg of olivine. *Frontiers in Climate*, *2*, 575744. https://doi.org/10.3389/fclim.2020.575744

Köhler, P. (2022). Plio-Pleistocene simulations from a global carbon cycle box model [Dataset]. PANGAEA. https://doi.org/10.1594/PANGAEA.940169

Köhler, P., & Bintanja, R. (2008). The carbon cycle during the mid Pleistocene transition: The Southern Ocean Decoupling Hypothesis. *Climate of the Past*, *4*, 311–332. https://doi.org/10.5194/cp-4-311-2008

Köhler, P., de Boer, B., von der Heydt, A. S., Stap, L. B., & van de Wal, R. S. W. (2015a). Model-based changes in global annual mean surface temperature change (Delta T_g) and radiative forcing due to land ice albedo changes (Delta $R_{[LI]}$) over the last 5 Myr, supplementary material [Dataset]. PANGAEA. https://doi.org/10.1594/PANGAEA.855449

Köhler, P., de Boer, B., von der Heydt, A. S., Stap, L. S., & van de Wal, R. S. W. (2015b). On the state dependency of equilibrium climate sensitivity during the last 5 million years. *Climate of the Past*, *11*(12), 1801–1823. https://doi.org/10.5194/cp-11-1801-2015

Köhler, P., & Fischer, H. (2004). Simulating changes in the terrestrial biosphere during the last glacial/interglacial transition. *Global and Planetary Change*, *43*(1–2), 33–55. https://doi.org/10.1016/j.gloplacha.2004.02.005

Köhler, P., & Fischer, H. (2006). Simulating low frequency changes in atmospheric CO_2 during the last 740000 years. *Climate of the Past*, *2*, 57–78. https://doi.org/10.5194/cp-2-57-2006

Köhler, P., Fischer, H., Munhoven, G., & Zeebe, R. E. (2005). Quantitative interpretation of atmospheric carbon records over the last glacial termination. *Global Biogeochemical Cycles*, *19*(4), GB4020. https://doi.org/10.1029/2004GB002345

Köhler, P., Fischer, H., & Schmitt, J. (2010). Atmospheric $\delta^{13}CO_2$ and its relation to pCO_2 and deep ocean $\delta^{13}C$ during the late Pleistocene. *Paleoceanography*, *25*(1), PA1213. https://doi.org/10.1029/2008PA001703

Köhler, P., & Munhoven, G. (2020a). Data to carbon cycle model simulations for the late Pleistocene by considering solid Earth processes [Dataset]. PANGAEA. https://doi.org/10.1594/PANGAEA.919146

Köhler, P., & Munhoven, G. (2020b). Late Pleistocene carbon cycle revisited by considering solid Earth processes. *Paleoceanography and Paleoclimatology*, *35*(12), e2020PA004020. https://doi.org/10.1029/2020PA004020

Köhler, P., & van de Wal, R. S. W. (2020). Interglacials of the Quaternary defined by northern hemispheric land ice distribution outside of Greenland. *Nature Communications*, *11*(1), 5124. https://doi.org/10.1038/s41467-020-18897-5

Komar, N., & Zeebe, R. E. (2021). Reconciling atmospheric CO_2, weathering, and calcite compensation depth across the Cenozoic. *Science Advances*, *7*(4), eabd4876. https://doi.org/10.1126/sciadv.abd4876

Kurahashi-Nakamura, T., Paul, A., Merkel, U., & Schulz, M. (2022). Glacial state of the global carbon cycle: Time-slice simulations for the last glacial maximum with an Earth-system model. *Climate of the Past*, *18*(9), 1997–2019. https://doi.org/10.5194/cp-18-1997-2022

Linsley, B. K., Dunbar, R. B., Dassié, E. P., Tangri, N., Wu, H. C., Brenner, L. D., & Wellington, G. M. (2019). Coral carbon isotope sensitivity to growth rate and water depth with paleo-sea level implications. *Nature Communications*, *10*(1), 2056. https://doi.org/10.1038/s41467-019-10054-x

Lisiecki, L. E. (2014). Atlantic overturning responses to obliquity and precession over the last 3 Myr. *Paleoceanography*, *29*(2), 71–86. https://doi.org/10.1002/2013PA002505

Lisiecki, L. E., & Raymo, M. E. (2005). A Pliocene-Pleistocene stack of 57 globally distributed benthic $\delta^{18}O$ records. *Paleoceanography*, *20*(1), PA1003. https://doi.org/10.1029/2004PA001071

Martínez-Botí, M. A., Foster, G. L., Chalk, T. B., Rohling, E. J., Sexton, P. F., Lunt, D. J., et al. (2015). Plio-Pleistocene climate sensitivity evaluated using high-resolution CO_2 records. *Nature*, *518*(7537), 49–54. https://doi.org/10.1038/nature14145

Martinez-Garcia, A., Rosell-Mele, A., Jaccard, S. L., Geibert, W., Sigman, D. M., & Haug, G. H. (2011). Southern Ocean dust-climate coupling over the past four million years. *Nature*, *476*(7360), 312–315. https://doi.org/10.1038/nature10310

Meissner, K. J., Schmittner, A., Weaver, A. J., & Adkins, J. F. (2003). Ventilation of the North Atlantic ocean during the last glacial maximum: A comparison between simulated and observed radiocarbon ages. *Paleoceanography*, *18*(2), 1023. https://doi.org/10.1029/2002PA000762

Menviel, L., Yu, J., Joos, F., Mouchet, A., Meissner, K. J., & England, M. H. (2017). Poorly ventilated deep ocean at the last glacial maximum inferred from carbon isotopes: A data-model comparison study. *Paleoceanography*, *32*(1), 2–17. https://doi.org/10.1002/2016PA003024

Mojica Prieto, F. J., & Millero, F. J. (2002). The values of $pK_1 + pK_2$ for the dissolution of carbonic acid in seawater. *Geochimica et Cosmochimica Acta*, *66*(14), 2529–2540. https://doi.org/10.1016/S0016-7037(02)00855-4

Phelps, S. R., Stoll, H. M., Bolton, C. T., Beaufort, L., & Polissar, P. J. (2021). Controls on alkenone carbon isotope fractionation in the modern ocean. *Geochemistry, Geophysics, Geosystems*, *22*(12), e2021GC009658. https://doi.org/10.1029/2021GC009658

Poore, H. R., Samworth, R., White, N. J., Jones, S. M., & McCave, I. N. (2006). Neogene overflow of northern component water at the Greenland-Scotland ridge. *Geochemistry, Geophysics, Geosystems*, *7*(6), Q06010. https://doi.org/10.1029/2005GC001085

Rae, J. W., Zhang, Y. G., Liu, X., Foster, G. L., Stoll, H. M., & Whiteford, R. D. (2021). Atmospheric CO_2 over the past 66 million years from marine archives. *Annual Review of Earth and Planetary Sciences*, *49*(1), 609–641. https://doi.org/10.1146/annurev-earth-082420-063026

Raymo, M. E. (1994). The initiation of northern hemisphere glaciation. *Annual Review of Earth and Planetary Sciences*, 22(1), 353–383. https://doi.org/10.1146/annurev.ea.22.050194.002033

Sarnthein, M., Pflaumann, U., & Weinelt, M. (2003). Past extent of sea ice in the northern North Atlantic inferred from foraminiferal paleotemperature estimates. *Paleoceanography*, *18*(2), 1047. https://doi.org/10.1029/2002PA000771

Schlitzer, R. (2000). Applying the adjoint method for biogeochemical modelling: Export of particulate organic matter in the world ocean, *Inverse methods in Global Biogeochemical Cycles. Geophysical Monographs*, *114*, 107–124. https://doi.org/10.1029/GM114p0107

Seki, O., Foster, G. L., Schmidt, D. N., Mackensen, A., Kawamura, K., & Pancost, R. D. (2010). Alkenone and boron-based Pliocene pCO_2 records. *Earth and Planetary Science Letters*, *292*(1–2), 201–211. https://doi.org/10.1016/j.epsl.2010.01.037

Shuttleworth, R., Bostock, H., Chalk, T., Calvo, E., Jaccard, S., Pelejero, C., et al. (2021). Early deglacial CO_2 release from the Sub-Antarctic Atlantic and Pacific oceans. *Earth and Planetary Science Letters*, *554*, 116649. https://doi.org/10.1016/j.epsl.2020.116649

Sosdian, S., Greenop, R., Hain, M., Foster, G., Pearson, P., & Lear, C. (2018). Constraining the evolution of Neogene ocean carbonate chemistry using the boron isotope pH proxy. *Earth and Planetary Science Letters*, *498*, 362–376. https://doi.org/10.1016/j.epsl.2018.06.017

Sosdian, S. M., Rosenthal, Y., & Toggweiler, J. R. (2018). Deep Atlantic carbonate ion and $CaCO_3$ compensation during the ice ages. *Paleoceanography and Paleoclimatology*, *33*(6), 546–562. https://doi.org/10.1029/2017PA003312

Stap, L. B., van de Wal, R. S. W., de Boer, B., Köhler, P., Hoencamp, J. H., Lohmann, G., et al. (2018a). Modeled influence of land ice and CO_2 on polar amplification and paleoclimate sensitivity during the past 5 million years. *Paleoceanography and Paleoclimatology*, *33*(4), 381–394. https://doi.org/10.1002/2017PA003313

Stap, L. B., van de Wal, R. S. W., de Boer, B., Köhler, P., Hoencamp, J. H., Lohmann, G., et al. (2018b). Simulation of northern hemispheric, southern hemispheric and global temperature over the past 5 million years [Dataset]. PANGAEA. https://doi.org/10.1594/PANGAEA.887427

Terhaar, J., Frölicher, T. L., & Joos, F. (2021). Southern Ocean anthropogenic carbon sink constrained by sea surface salinity. *Science Advances*, *7*(18), eabd5964. https://doi.org/10.1126/sciadv.abd5964

Tierney, J. E., Zhu, J., King, J., Malevich, S. B., Hakim, G. J., & Poulsen, C. J. (2020). Glacial cooling and climate sensitivity revisited. *Nature*, *584*(7822), 569–573. https://doi.org/10.1038/s41586-020-2617-x

Tyrrell, T., & Zeebe, R. E. (2004). History of carbonate ion concentration over the last 100 million years. *Geochimica et Cosmochimica Acta*, *68*(17), 3521–3530. https://doi.org/10.1016/j.gca.2004.02.018

Völker, C., & Köhler, P. (2013). Responses of ocean circulation and carbon cycle to changes in the position of the Southern hemisphere westerlies at Last Glacial Maximum. *Paleoceanography*, *28*(4), 726–739. https://doi.org/10.1002/2013PA002556

Willeit, M., Ganopolski, A., Calov, R., & Brovkin, V. (2019). Mid-Pleistocene transition in glacial cycles explained by declining CO_2 and regolith removal. *Science Advances*, *5*(4), eaav7337. https://doi.org/10.1126/sciadv.aav7337

Yamamoto, M., Clemens, S. C., Seki, O., Tsuchiya, Y., Huang, Y., O'ishi, R., & Abe-Ouchi, A. (2022). Increased interglacial atmospheric CO_2 levels followed the mid-Pleistocene Transition. *Nature Geoscience*, *15*(4), 307–313. https://doi.org/10.1038/s41561-022-00918-1

Yan, Y., Bender, M. L., Brook, E. J., Clifford, H. M., Kemeny, P. C., Kurbatov, A. V., et al. (2019). Two-million-year-old snapshots of atmospheric gases from Antarctic ice. *Nature*, *574*(7780), 663–666. https://doi.org/10.1038/s41586-019-1692-3

Yu, J., Anderson, R. F., Jin, Z., Rae, J. W., Opdyke, B. N., & Eggins, S. M. (2013). Responses of the deep ocean carbonate system to carbon reorganization during the Last Glacial-interglacial cycle. *Quaternary Science Reviews*, *76*(0), 39–52. https://doi.org/10.1016/j.quascirev.2013.06.020

Zeebe, R. E. (2012). LOSCAR: Long-term Ocean-atmosphere-Sediment CArbon cycle Reservoir model v2.0.4. *Geoscientific Model Development*, *5*(1), 149–166. https://doi.org/10.5194/gmd-5-149-2012

Zeebe, R. E., & Tyrrell, T. (2019). History of carbonate ion concentration over the last 100 million years II: Revised calculations and new data. *Geochimica et Cosmochimica Acta*, *257*, 373–392. https://doi.org/10.1016/j.gca.2019.02.041

Zeebe, R. E., & Wolf-Gladrow, D. A. (2001). CO_2 in seawater: Equilibrium, kinetics, isotopes. *Elsevier Oceanography Book Series* (Vol. 65). Elsevier Science Publishing.

Zhang, Y. G., Pagani, M., Liu, Z., Bohaty, S. M., & DeConto, R. (2013). A 40-million-year history of atmospheric CO_2. *Philosophical Transactions of the Royal Society A: Mathematical, Physical & Engineering Sciences*, *371*(2001), 20130096. https://doi.org/10.1098/rsta.2013.0096

Zhang, Y. G., Pearson, A., Benthien, A., Dong, L., Huybers, P., Liu, X., & Pagani, M. (2019). Refining the alkenone-pCO_2 method I: Lessons from the Quaternary glacial cycles. *Geochimica et Cosmochimica Acta*, *260*, 177–191. https://doi.org/10.1016/j.gca.2019.06.032

Zhang, Z., Li, X., Guo, C., Otterå, O. H., Nisancioglu, K. H., Tan, N., et al. (2021). Mid-Pliocene Atlantic meridional overturning circulation simulated in PlioMIP2. *Climate of the Past*, *17*(1), 529–543. https://doi.org/10.5194/cp-17-529-2021

Zhou, X., Rosenthal, Y., Haynes, L., Si, W., Evans, D., Huang, K.-F., et al. (2021). Planktic foraminiferal Na/Ca: A potential proxy for seawater calcium concentration. *Geochimica et Cosmochimica Acta*, *305*, 306–322. https://doi.org/10.1016/j.gca.2021.04.012

Supporting Information for "Atmospheric CO$_2$ concentration based on boron isotopes versus simulations of the global carbon cycle during the Plio-Pleistocene"

Peter Köhler[1]

[1] Alfred-Wegener-Institut Helmholtz-Zentrum für Polar-und Meeresforschung (AWI)

P.O. Box 12 01 61, 27515 Bremerhaven, Germany

Contents of this file
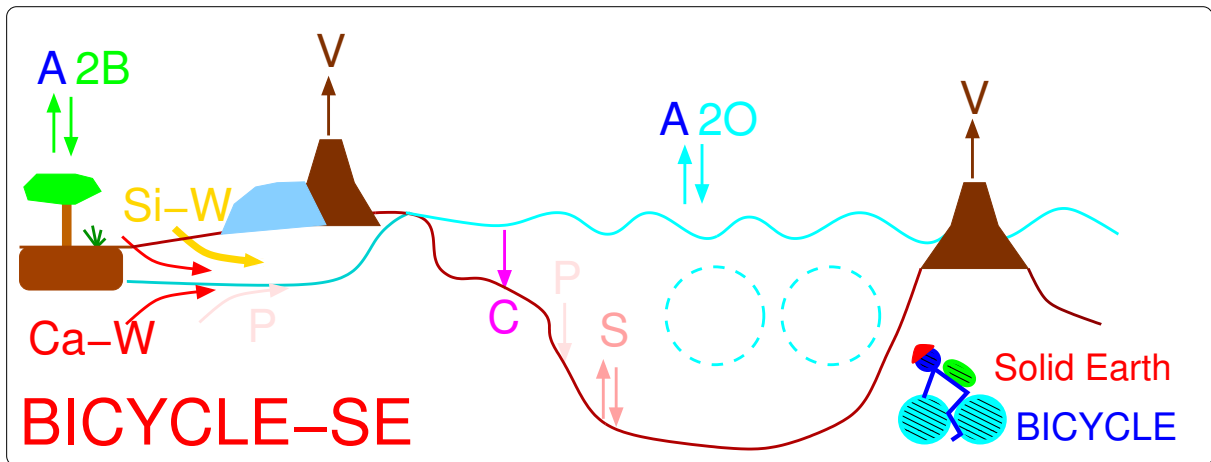
Figure S1. Sketch of the BICYCLE model. Model version including solid Earth fluxes (BICYCLE-SE). V: outgassing of CO_2 from volcanoes on land potentially and temporally overlain by land ice and from hot spot island volcanoes (and mid ocean ridges, not shown) influenced by changing sea level; C: shallow water carbonate deposition due to coral reef growth; Si-W: silicate weathering and Ca-W: carbonate weathering with different sources of C, but both delivering HCO_3^--ions into the ocean; P: PO_4^{3-} riverine input and sedimentary burial; S: $CaCO_3$ sedimentation and dissolution. A2B: atmosphere-biosphere exchange of CO_2; A2O: atmosphere-ocean exchange of CO_2. The cyan-colored broken circles mimic the two overturning cells in the Atlantic and Indo-Pacific Ocean. The previous model version has been restricted to the fluxes A2O, A2B, and some simplified representation of carbonate compensation between ocean and sediment.
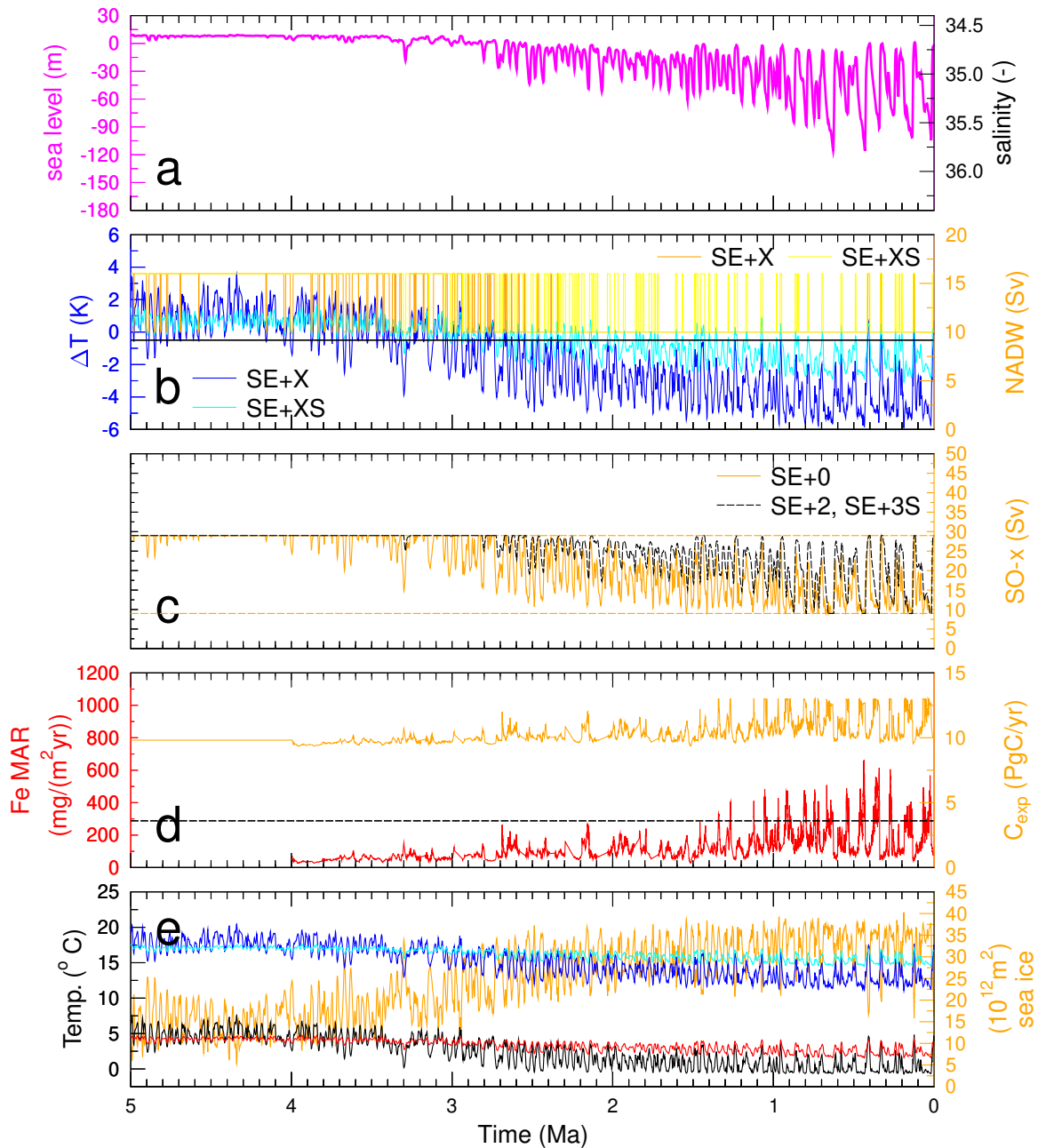
Figure S2. Time-dependent forcing of the model. (a) Sea level following *de Boer et al.* [2014] resulting in the corresponding mean ocean salinity (right y-axis). (b) North Atlantic Deep Water (NADW) formation is either in interglacial or glacial mode, following NH high latitude SST, broken line marks the threshold for switching between both states. (c) SH high latitude SST and vertical mixing (SO-x: SO surface-to-deep ocean flux, right y-axis) is calculated with upper and lower limitation (9–29 Sv), marked by horizontal lines. In scenario SE+2 the vertical mixing is calculated as function of sea level. (d) Marine biology in the Southern Ocean (SO) is either Fe-limited or Fe-unlimited following Fe MAR in ODP1090 [*Martinez-Garcia et al.*, 2011]. The dotted line marks the threshold for switching between both states, leading to global integrated export production of organic matter at 100 m water depth (right y-axis). (e) Different ocean temperatures averaged within the model (mean ocean (black (standard), red (alternative))). SST is calculated from all ocean surface boxes (area weighted (blue (standard), cyan (alternative)). Right y-axis: global integrated sea ice area (std). The standard run is forced with temperature from *Köhler et al.* [2015], the alternative with temperature from *Stap et al.* [2018].
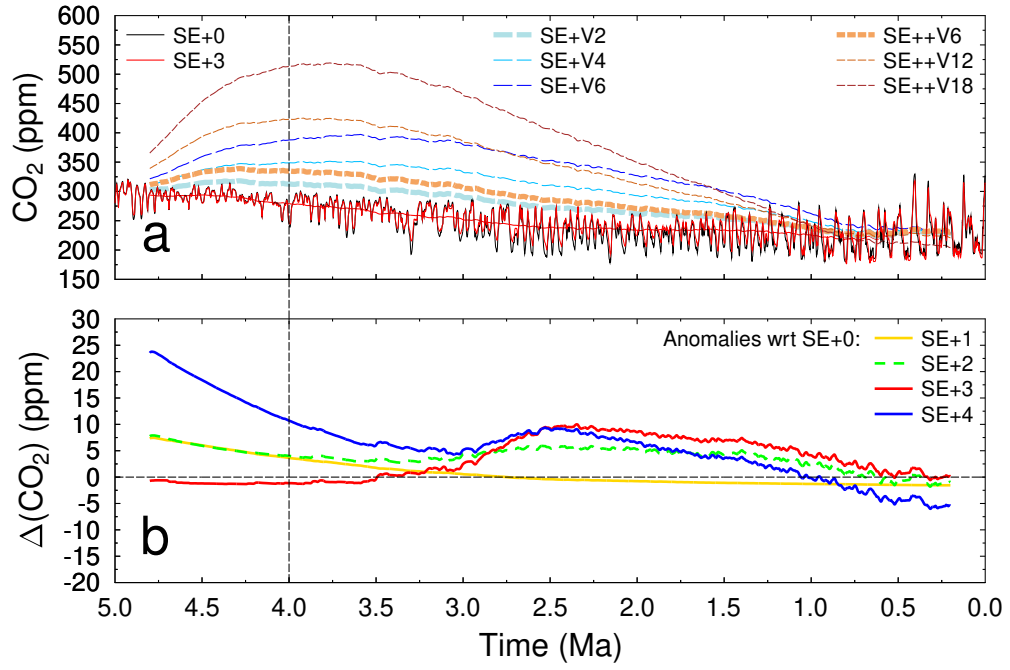
Figure S3. Simulated atmospheric CO_2 for different scenarios (a) and anomalies of some scenarios with respect to SE+0 (b). Most time series are plotted as 400-ka running mean, for SE+0 and SE+3 the underlying raw data are also shown.
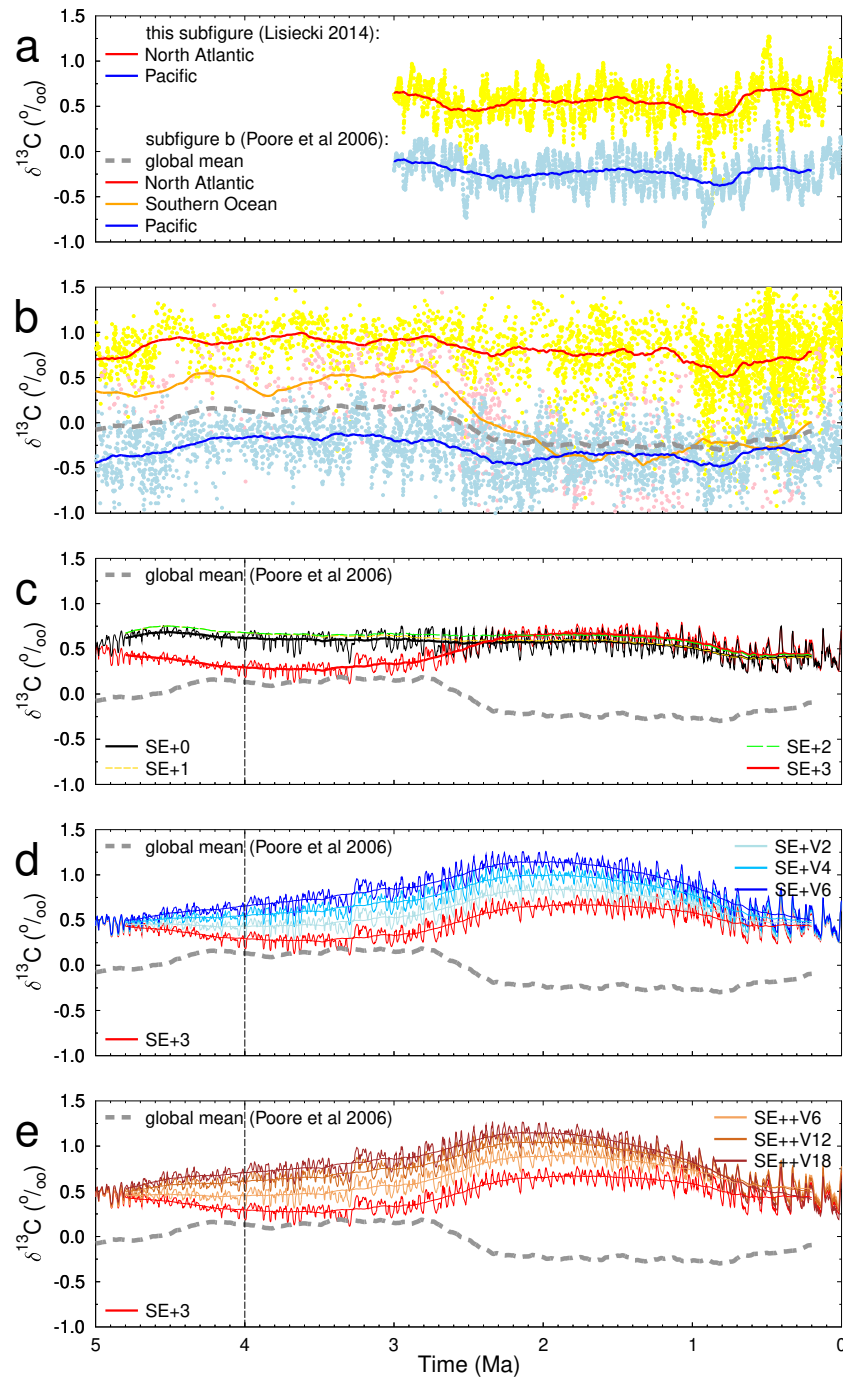
Figure S4. Oceanic δ^{13}C. (a) Mean δ^{13}C stack from the North Atlantic and Pacific after *Lisiecki* [2014]. (b) Mean δ^{13}C stack from the North Atlantic (NA), Southern Ocean (SO) and Pacific (PA) after *Poore et al.* [2006]. A 400-ka running mean of the global mean ocean δ^{13}C (gray line in sub-figures b–e) is calculated by averaging the three basin-wide records with weighting factors of 0.1 (NA), 0.32 (SO), and 0.58 (PA). These factors are based on the distribution of ocean volumes below 1000 m depth according to the model geometry. Because Atlantic δ^{13}C data are only obtained from the North Atlantic I have to assume how much of the deep Atlantic is ventilated by either northern or southern component waters. Here, a temporally constant northern component ventilation rate of 50% is assumed, but an alternative time-dependent weighting factor which takes the variability of the northern component waters into account as used in *Poore et al.* [2006] leads to very similar results. (c–e) Simulated mean ocean δ^{13}C in various scenarios versus the data-based global mean ocean δ^{13}C. Plotted results contain both raw data and 400-ka running mean changes.
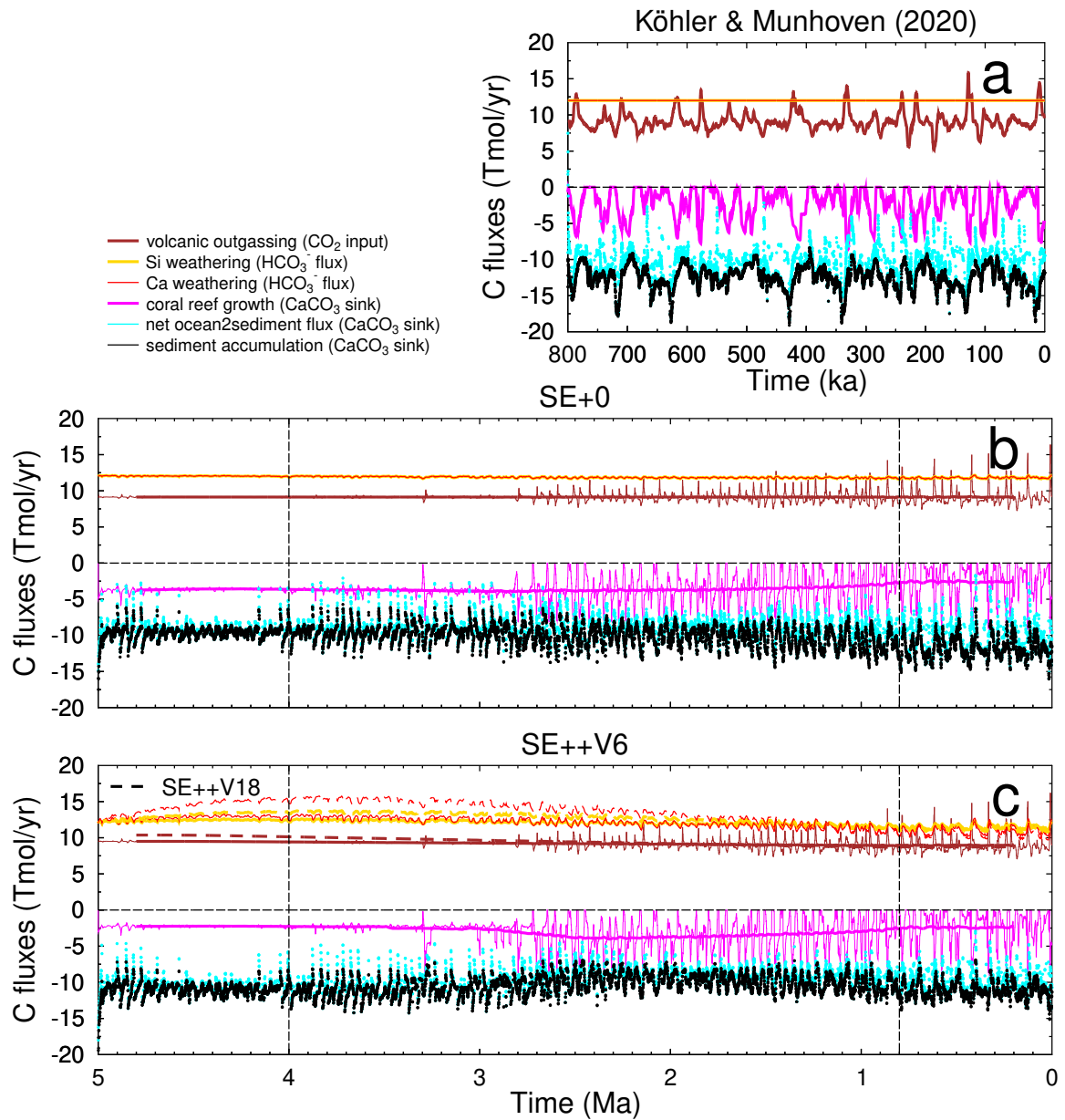
Figure S5. Contribution of solid Earth processes to changes in the global carbon cycle. (a) Standard run SE in *Köhler and Munhoven* [2020]. (b) Scenario SE+0. (c) Scenario SE++V6 (solid lines) and SE++V18 (broken lines). The relevant process and the carbon species that is changes is mentioned in the legend. All fluxes apart from the volcanic outgassing lead to changes in both the total carbon content in the atmosphere-ocean-biosphere subsystem and in the ocean alkalinity, (volcanic outgassing does not change ocean alkalinity). Calcite dissolution (sediment-to-ocean flux) is the difference between sediment accumulation and net ocean-to-sediment and omitted. Not all calcite dissolution events are resolved here due to a temporal resolution of the results of 1 ka.
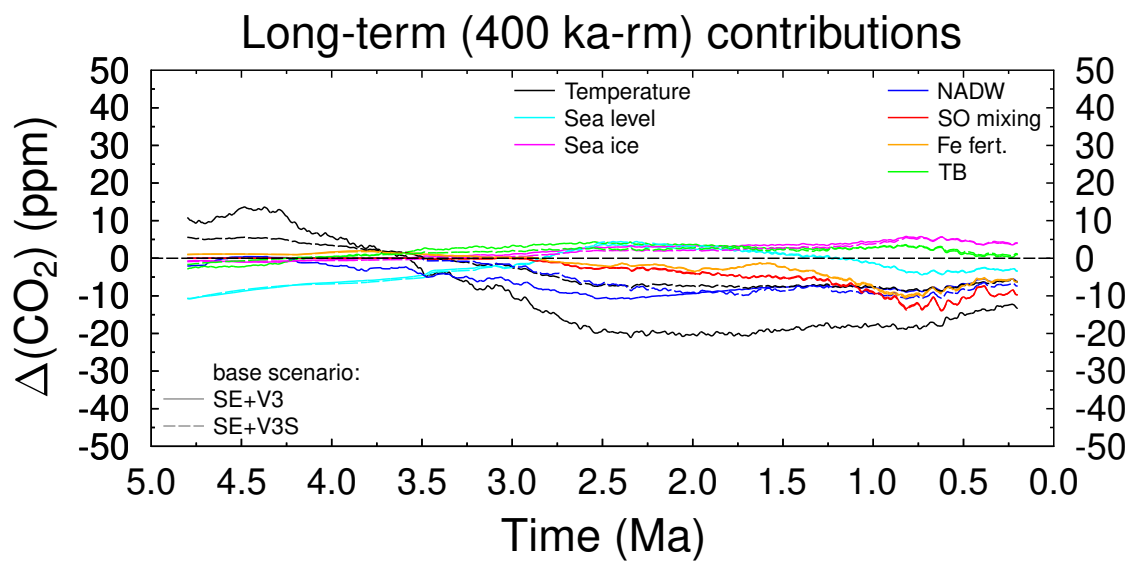
Figure S6. Contributions of different non-solid Earth processes to changes in atmospheric CO_2 for different base lines (SE+V3 vs SE+V3S). The investigated processes are ocean temperature, sea level, sea ice, strength of the North Atlantic Deep Water (NADW) formation, vertical mixing in the Southern Ocean (SO), iron fertilization in the Southern Ocean, and changes in the terrestrial biosphere (TB). All as 400-ka running mean.
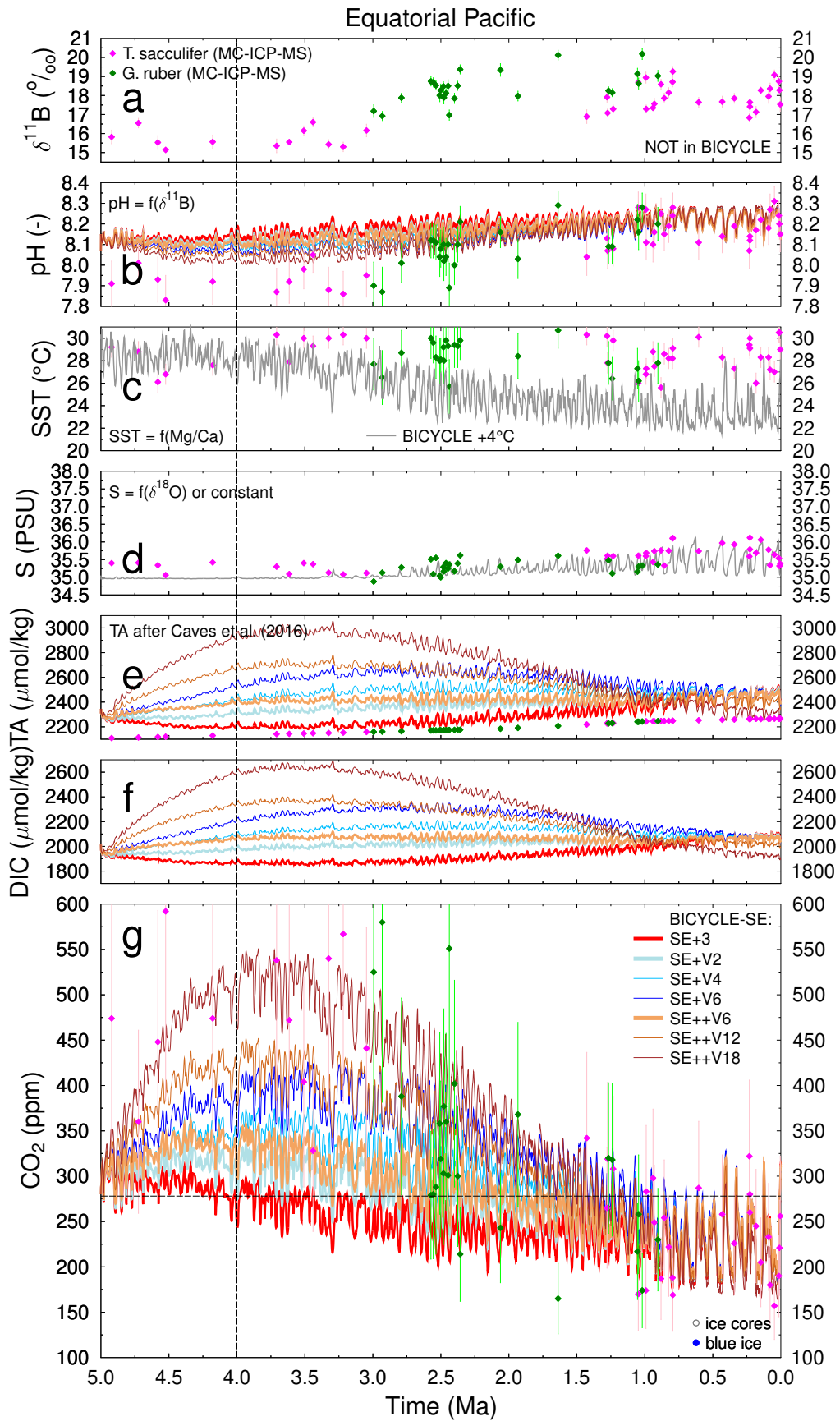
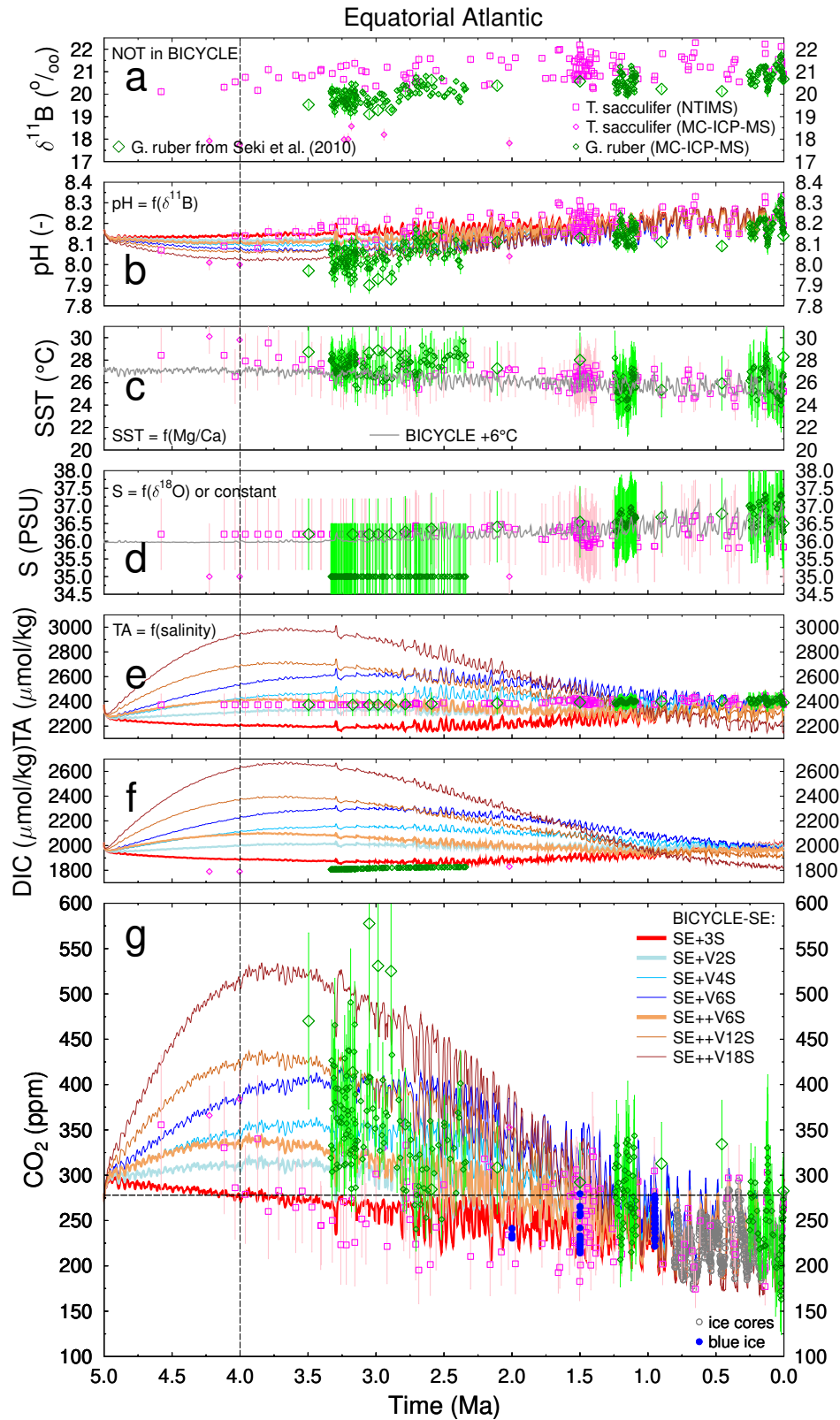**Figure S7.** Details on the δ^{11}B-based CO_2 proxies from the surface equatorial Pacific (see legends in subfigures a and g): (a) measured δ^{11}B; (b) pH; (c) SST; (d) salinity; (e) TA; (f) DIC; (g) atmospheric CO_2. Data as compiled in *Guillermic et al.* [2022] with additions of CO_2 from ice cores [*Bereiter et al.*, 2015] and blue ice [*Yan et al.*, 2019]. As 2nd variable of the carbonate system this study estimated TA. Whenever two errors are given in *Guillermic et al.* [2022] only "error 1" is shown and discussed, which contained a more complete error propagation than "error 2". All uncertainties are $\pm 1\sigma$.

Figure S8. Details on the δ^{11}B-based CO_2 proxies from the surface equatorial Atlantic (see legends in subfigures a and g) when forced by the alternative temperatures from *Stap et al.* [2018a]: (a) measured δ^{11}B; (b) pH; (c) SST; (d) salinity; (e) TA; (f) DIC; (g) atmospheric CO_2. Data as compiled in *Dyez et al.* [2018] with updates from *de la Vega et al.* [2020] and paleo-co2.org with additions of CO_2 from ice cores [*Bereiter et al.*, 2015] and blue ice [*Yan et al.*, 2019]. As 2nd variable of the carbonate system nearly all studies estimates TA, while *de la Vega et al.* [2020] estimates DIC. Data originally published in *Seki et al.* [2010] are marked with different symbols, since they contain the unusual high CO_2 values around 3 Ma. All uncertainties are ±1σ.
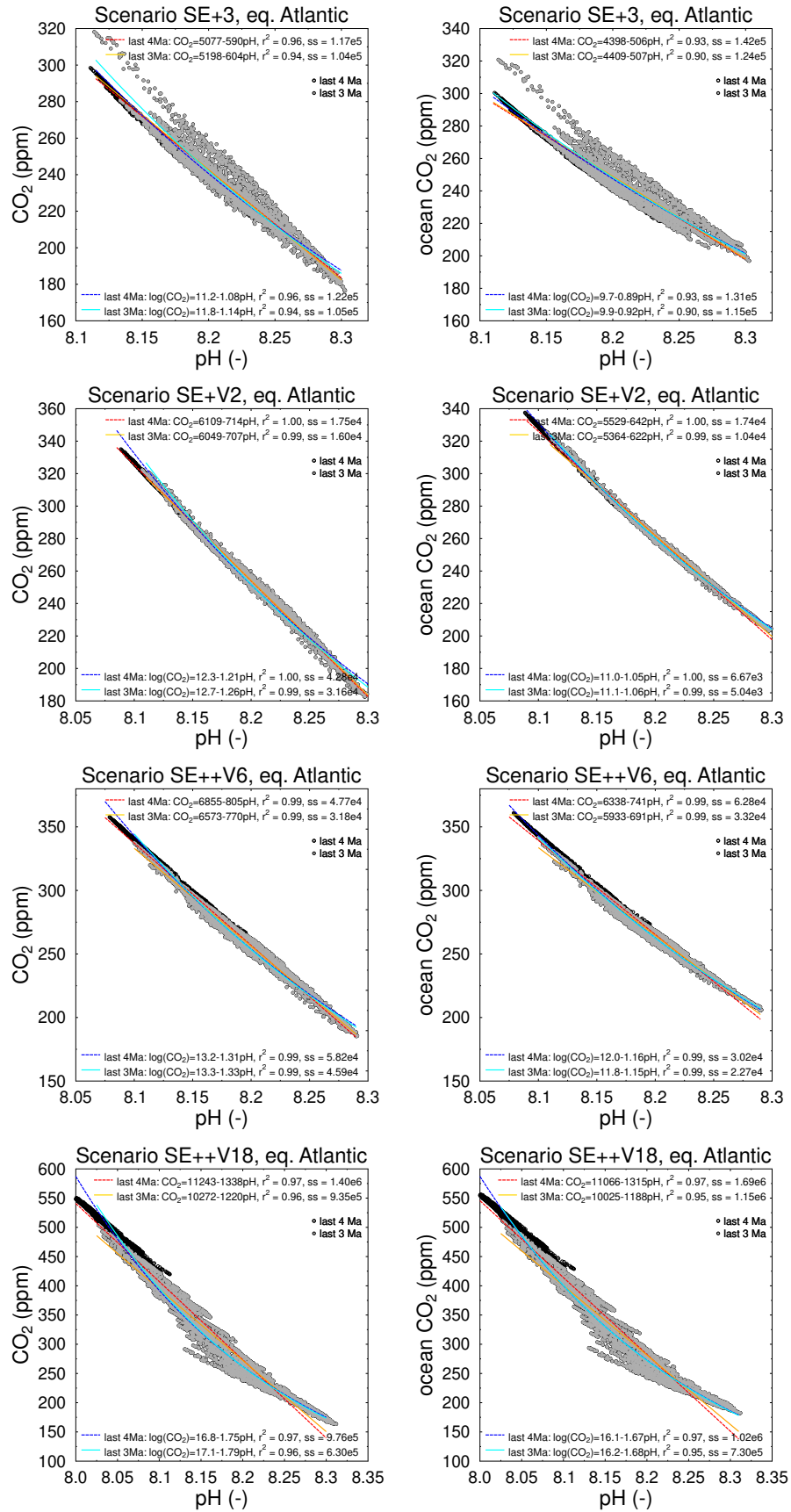
Figure S9. Linear regression plots for selected scenarios between atmospheric CO_2 (left) or surface equatorial Atlantic CO_2 (right) and pH in the surface equatorial Atlantic. In the lower left corner the calculated regression functions are given, if, as suggested [*Hain et al.*, 2018b] the logarithm of atmospheric CO_2 is calculated as function of surface equatorial Atlantic pH. *ss* is the calculated sum of squares, which indicates if the linear or logarithmic fit performs better.
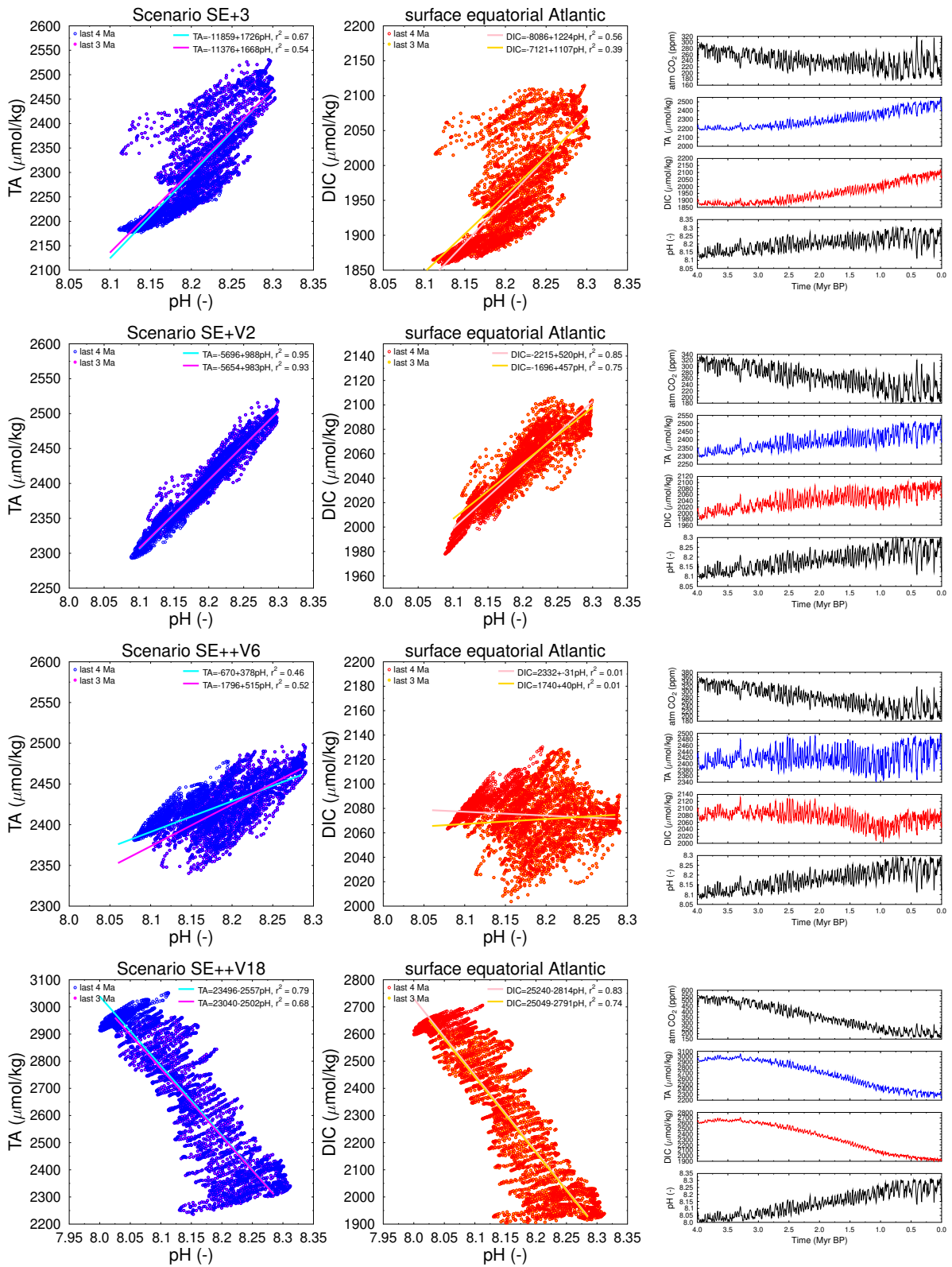
Figure S10. Linear regression plots for selected scenarios between atmospheric pH and (left) DIC or (right) TA in the surface equatorial Atlantic for selected scenarios (SE+3: 1st row; SE+V2: 2nd row; SE++V6 3rd row: SE++V18 4th row). Right column contains the related time series including one for atmospheric CO_2.
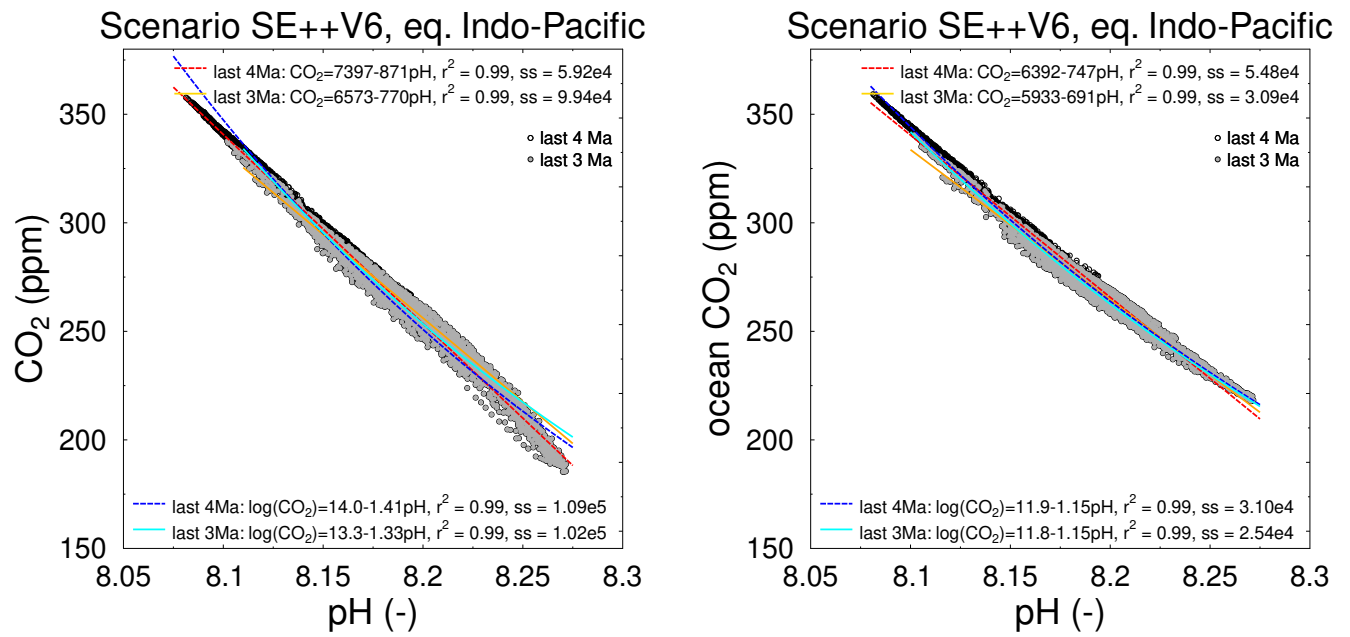
Figure S11. Example of a linear regression plot between between atmospheric CO_2 (left) or surface equatorial Indo-Pacific CO_2 (right) and pH in the surface equatorial Indo-Pacific for scenario SE++V6. In the lower left corner the calculated regression functions are given, if, as suggested [*Hain et al.*, 2018b] the logarithm of atmospheric CO_2 is calculated as function of surface equatorial Atlantic pH. *ss* is the calculated sum of squares, which indicates if the linear or logarithmic fit performs better.
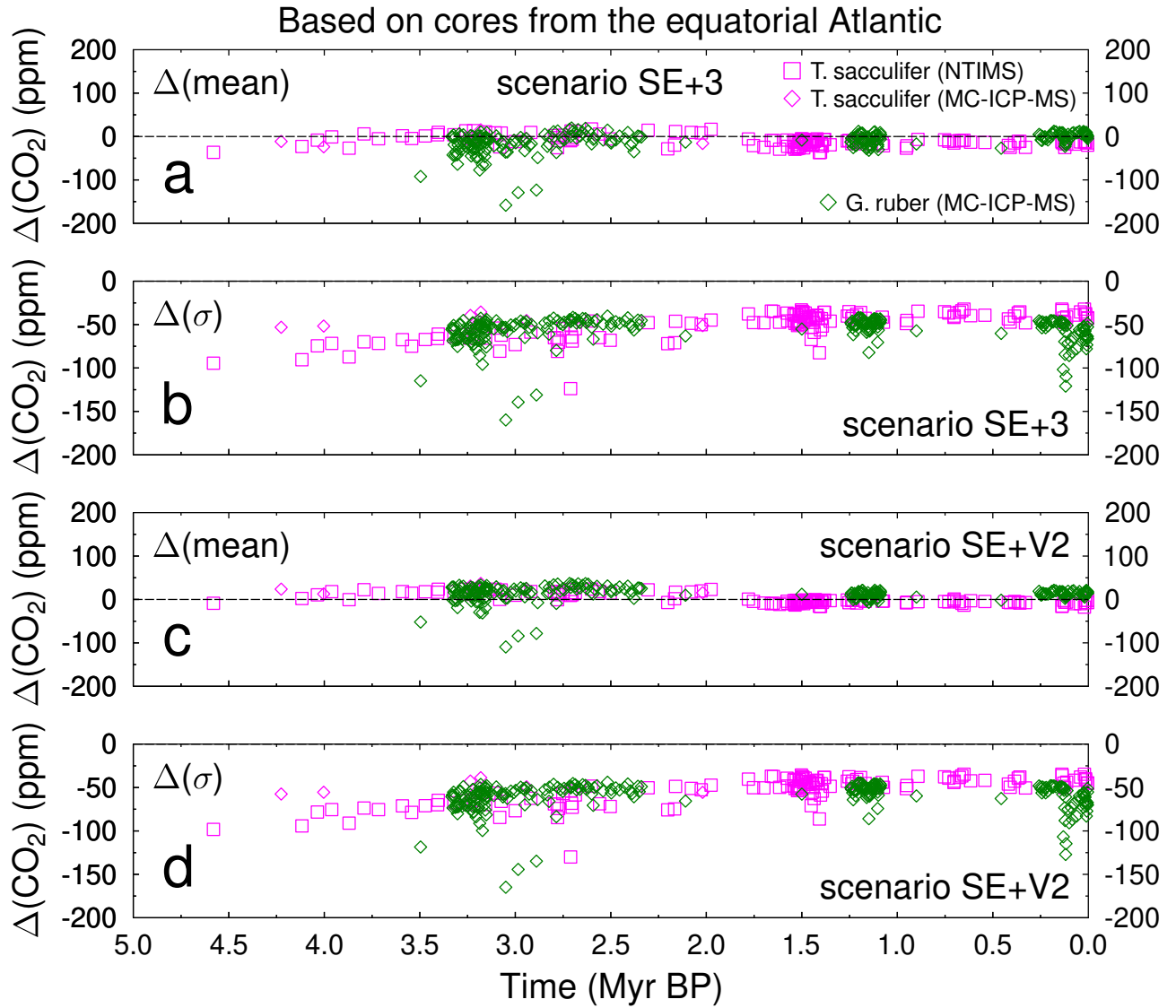
Figure S12. Calculating atmospheric CO_2 out of δ^{11}B-based pH using linear regressions for selected scenarios (a,b) scenario SE+3; (c,d) scenario SE+V2. I use the linear regressions as obtained between equatorial surface Atlantic pH and atmospheric CO_2 from 4 Ma data (Fig. S9). Plotted are changes in the mean values (a,c) and of the uncertainties (b,d) in atmospheric CO_2. The differences are always plotted as new calculated values minus originally reconstructed values.
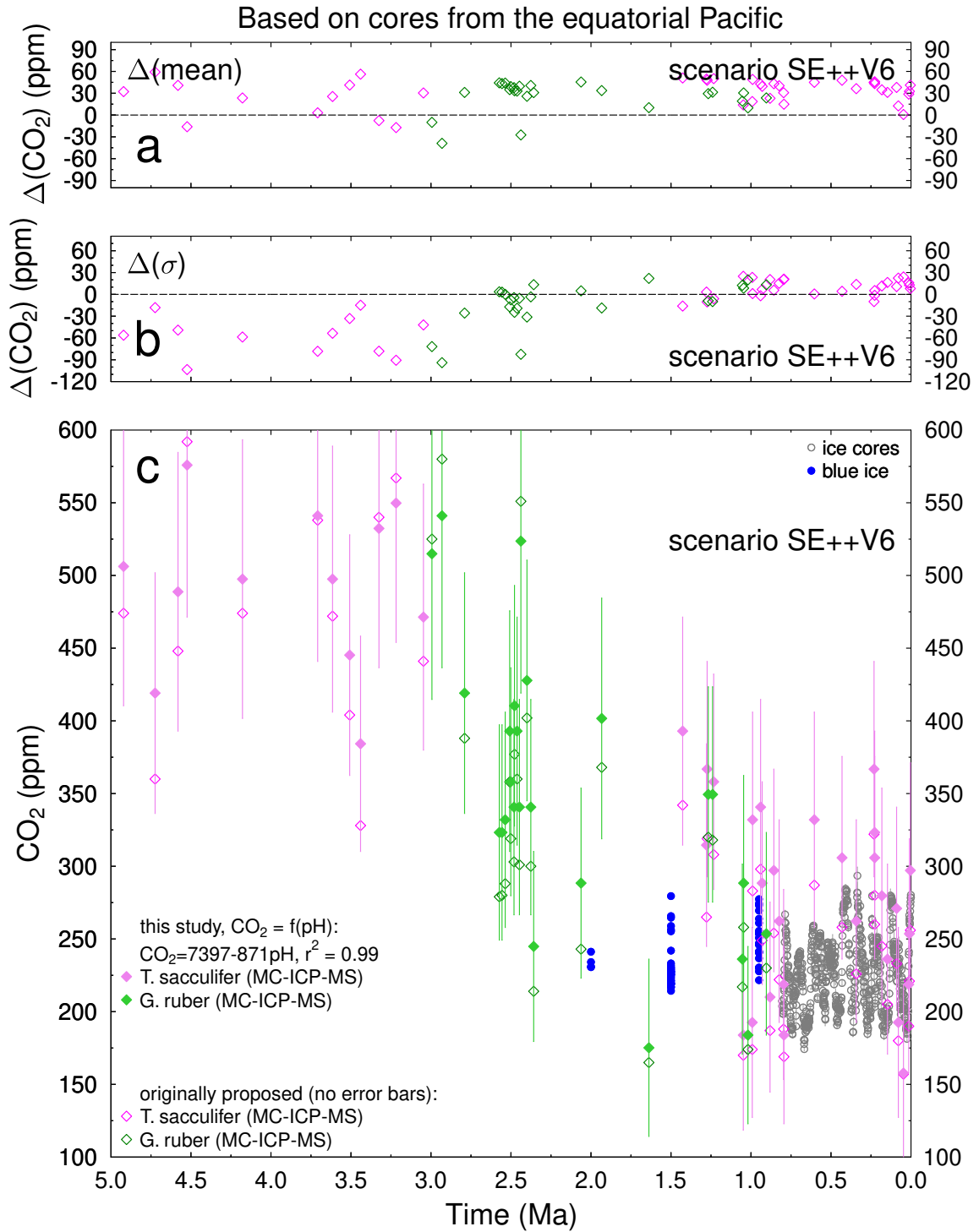
Figure S13. Calculating atmospheric CO_2 out of $\delta^{11}B$-based pH using linear regressions for scenario SE++V6 based on core site in the equatorial Pacific [*Guillermic et al.*, 2022]. Changes in the mean values (a) and of the uncertainties (b), and comparing original proposed and newly calculated atmospheric CO_2 (c) with additions of CO_2 from ice cores [*Bereiter et al.*, 2015] and blue ice [*Yan et al.*, 2019]. I use the linear regressions between pH and CO_2 as obtained from 4 Ma data. The differences are always plotted as new calculated values minus originally reconstructed values.
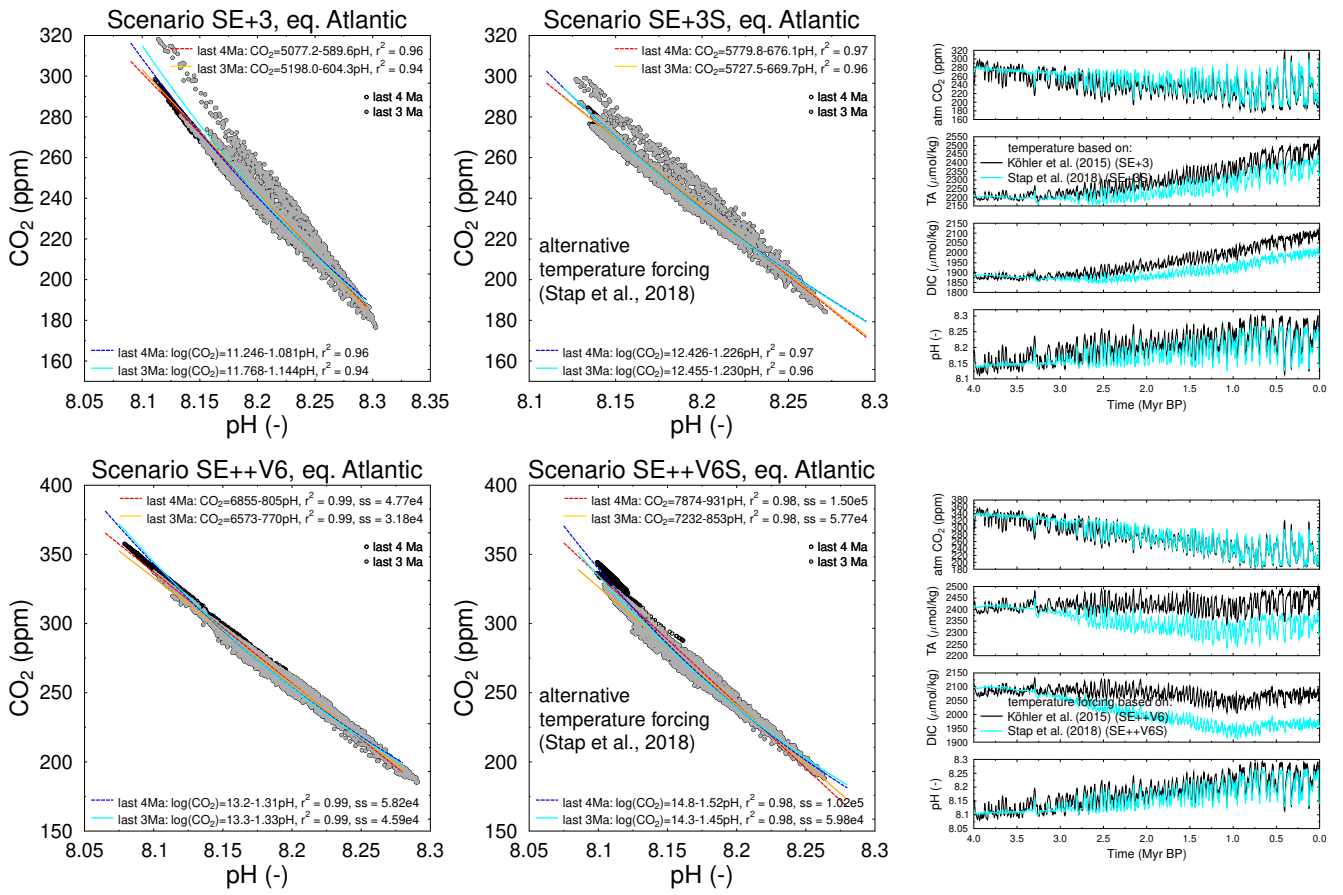
Figure S14. Example of a linear regression plot between atmospheric CO_2 and pH in the surface equatorial Atlantic for the scenarios SE+3 (top) and SE++V6 (bottom), in comparison to scenarios (SE+3S, SE++V6S) which use the alternative temperature forcing following *Stap et al.* [2018] . Right column contains the related time series for for atmospheric CO_2 and surface equatorial Atlantic pH, TA, and DIC.